



Brain capillary pericytes exert a substantial but slow influence on blood flow

David A. Hartmann^{1,2}, Andrée-Anne Berthiaume^{1,3}, Roger I. Grant¹, Sarah A. Harrill¹, Tegan Koski¹, Taryn Tieu³, Konnor P. McDowell^{1,3}, Anna V. Faino⁴, Abigail L. Kelly⁵ and Andy Y. Shih^{1,3,6,7} ✉

The majority of the brain's vasculature is composed of intricate capillary networks lined by capillary pericytes. However, it remains unclear whether capillary pericytes influence blood flow. Using two-photon microscopy to observe and manipulate brain capillary pericytes in vivo, we find that their optogenetic stimulation decreases lumen diameter and blood flow, but with slower kinetics than similar stimulation of mural cells on upstream pial and precapillary arterioles. This slow vasoconstriction was inhibited by the clinically used vasodilator fasudil, a Rho-kinase inhibitor that blocks contractile machinery. Capillary pericytes were also slower to constrict back to baseline following hypercapnia-induced dilation, and slower to dilate towards baseline following optogenetically induced vasoconstriction. Optical ablation of single capillary pericytes led to sustained local dilation and a doubling of blood cell flux selectively in capillaries lacking pericyte contact. These data indicate that capillary pericytes contribute to basal blood flow resistance and slow modulation of blood flow throughout the brain.

The adult human brain contains more than 400 miles of vasculature, tasked with delivery of oxygen and nutrients to billions of brain cells. Understanding how the cerebrovasculature achieves this feat is critical because insufficient blood flow contributes to pathology in numerous neurologic conditions including stroke, vascular cognitive impairment and Alzheimer's disease¹. The distribution of blood relies on a dense capillary network, through which all red blood cells (RBCs) percolate single-file during their transit from arteries to veins². With this arrangement, it is no surprise that the capillary bed possesses the highest flow resistance within the cerebrovasculature³. This flow resistance must be carefully tuned for proper allocation of blood to all regions of the brain. However, the factors that govern capillary blood flow in the brain remain largely unknown.

Collectively referred to as vascular mural cells, smooth muscle cells (SMCs) and pericytes line the entire cerebrovasculature, but occupy distinct microvascular zones⁴. On arterioles, concentric rings of SMCs produce powerful constrictions or dilations to rapidly alter blood supply. These SMC dynamics are critical for blood flow control during neurovascular coupling, where fluctuating neuronal activity produces commensurate changes in blood supply within seconds (ref. ⁵). Meanwhile, pericytes are the predominant mural cell form in capillary networks. Pericytes are characterized by protruding ovoid cell bodies and long, thin processes that partially cover the capillary surface. Their shared embryology with SMCs as well as their anatomical location within the capillary basement membrane have led many to hypothesize that pericytes modulate blood flow at the capillary level⁶. However, this hypothesis has remained controversial since pericytes were discovered. Pioneering *ex vivo* rodent brain slice studies first demonstrated that brain pericytes could alter capillary diameter in response to electrical stimulation, neurotransmitters and ischemia⁷. Yet, studies seeking to corroborate these responses *in vivo* have resulted in mixed out-

comes, with some studies supporting modulation of capillary blood flow by brain pericytes^{8–10}, and others reporting the contrary^{5,11,12}.

Two salient issues underlie the conflicting reports from *in vivo* studies. First, at least three unique mural cell forms reside on brain arterioles, precapillary arterioles and capillaries⁴. Mural cells that clearly control blood flow are SMCs on arterioles and ensheathing pericytes on precapillary arterioles⁵. Both cell types completely encircle the vessel lumen and express the contractile protein α -SMA. However, ensheathing pericytes are more elongated and have ovoid cell bodies that protrude from the vessel wall, which are traits that resemble classically described pericytes found on capillaries⁴ (note that ensheathing pericytes are synonymous with 'precapillary SMCs'⁵). In contrast, capillary pericytes of the capillary bed express low to undetectable levels of α -SMA unlike upstream mural cells⁴. Many previous studies have not semantically distinguished between ensheathing and capillary pericytes, fueling debate about whether capillary pericytes regulate blood flow. This is critical to clarify because capillary pericytes contact the vast majority of the cerebrovascular length and may therefore profoundly influence blood flow if indeed contractile. Further, the loss or dysfunction of capillary pericytes has been implicated in blood flow abnormalities found in stroke^{5,8,13}, dementia^{14–16}, epilepsy¹⁷ and spinal cord injury¹⁸.

The second issue in studying the role of capillary pericytes *in vivo* is the inherent connectivity of the cerebrovasculature. Since capillary blood flow dynamics are so greatly affected by upstream arterioles, the autonomous ability of capillary pericytes to control flow is difficult to discern using observational approaches. Several previous studies correlated local changes in capillary diameter with the presence (or absence) of pericyte somata^{8,9,11,12}. However, it is difficult to distinguish the influence of upstream flow changes using this approach. Further, these studies assume that only the soma of pericytes can exert tone on capillaries. Mouse models with selective genetic ablation of capillary pericytes do not necessarily solve

¹Department of Neuroscience, Medical University of South Carolina, Charleston, SC, USA. ²Department of Neurology & Neurological Sciences, Stanford University, Stanford, CA, USA. ³Center for Developmental Biology and Regenerative Medicine, Seattle Children's Research Institute, Seattle, WA, USA.

⁴Core for Biomedical Statistics, Seattle Children's Research Institute, Seattle, WA, USA. ⁵Public Health Sciences, Medical University of South Carolina, Charleston, SC, USA. ⁶Department of Pediatrics, University of Washington, Seattle, WA, USA. ⁷Department of Bioengineering, University of Washington, Seattle, WA, USA. ✉e-mail: Andy.Shih@SeattleChildrens.org

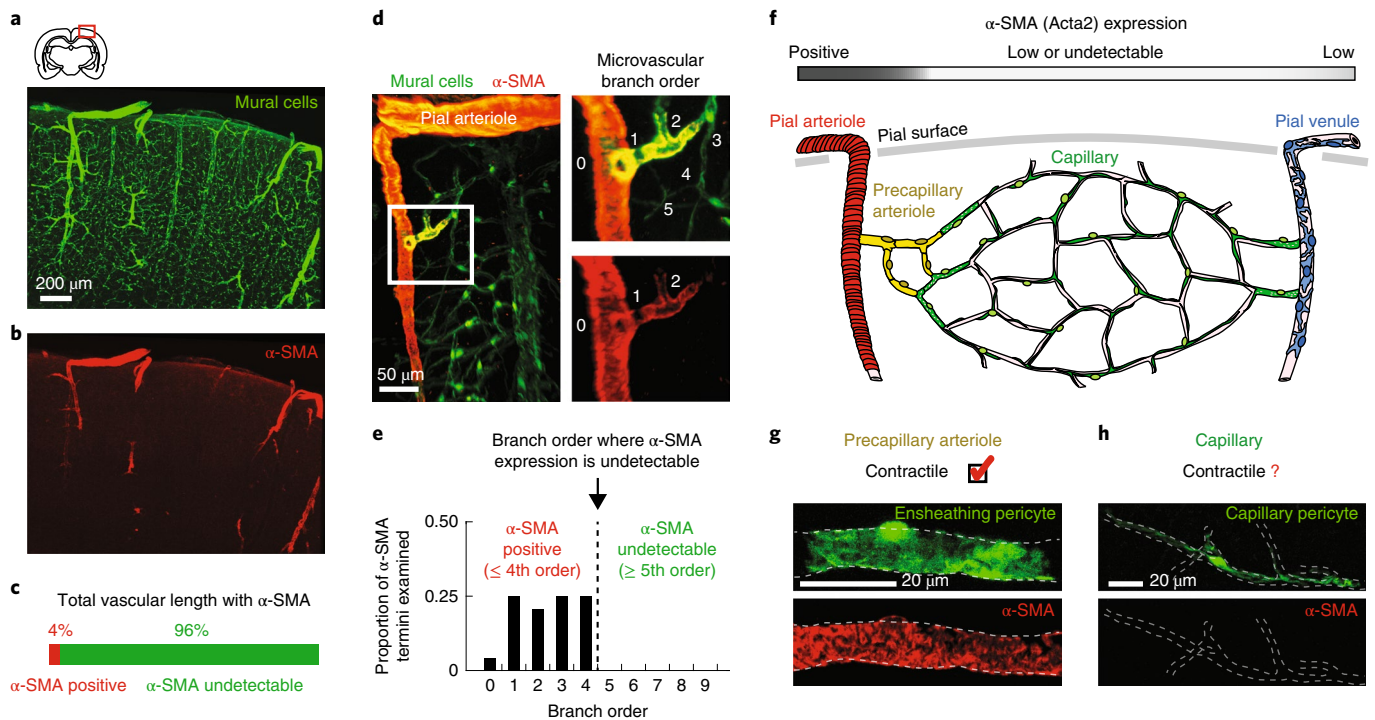


Fig. 1 | Capillary pericytes contact the vast majority of mouse cerebrovasculature. a, Thick tissue section from cerebral cortex showing genetically labeled mural cells (PDGFR β -tdTomato) in green. **b**, Immunostaining of α -SMA in red. **c**, Proportion of vascular length associated with α -SMA-positive mural cells (SMCs and ensheathing pericytes) versus α -SMA-low or α -SMA-undetectable mural cells (capillary pericytes). A total of 138 mm of cortical vascular length was quantified across four volumetric datasets from two mice. **d**, Drop in α -SMA expression as precapillary arterioles transition into capillaries. The inset shows a penetrating arteriole offshoot with α -SMA termination occurring at the second-order branch. **e**, Histogram showing proportion of branch orders at which α -SMA decrease occurs in the upper 350 μ m of cortex. $N = 24$ α -SMA termini (2 mice, 11 penetrating arteriole networks). **f**, Schematic depicting microvascular zones, with SMCs on pial and penetrating arterioles (red), ensheathing pericytes on precapillary arterioles (yellow), capillary pericytes on capillaries (green) and stellate SMCs on venules (blue). Expression of α -SMA decreases sharply between precapillary arteriole and capillary zones. **g, h**, Contractile ability is established for ensheathing pericytes (**g**), but remains uncertain for capillary pericytes (**h**).

this problem. In a recent study, deletion of large numbers of capillary pericytes in the adult brain led to reduced blood flow, but perhaps secondary to substantial blood–brain barrier breakdown and edema, rather than effects on pericyte tone¹⁹. Brain ischemia also produces capillary constriction that slows blood flow and contributes to infarct growth¹³. However, it can be difficult to discern whether pericytes or other factors such as edema are the basis of capillary constriction. Thus, ‘cause-and-effect’ studies that manipulate capillary pericytes in a cell-specific manner are needed to fully understand their effect on blood flow in vivo during health and disease.

In this study, we examine whether capillary pericytes provide vascular tone and flow resistance in vivo. We overcome earlier issues of pericyte identification by making careful distinctions between microvascular zones of adult mouse cortex, and by using cell morphology and vascular branch order criteria to unambiguously identify capillary pericytes in vivo. Further, we study capillary pericytes in a cause-and-effect manner by using spatially localized two-photon optical manipulations to either stimulate or ablate individual capillary pericytes. This disentangles their local influence on capillary hemodynamics from the influence of flow in upstream vessels.

Results

Distinguishing the different mural cells of precapillary and capillary zones. We bred PDGFR β -Cre mice with fluorescent reporter mice to achieve robust fluorescent labeling of mural cells throughout the cerebrovasculature (Fig. 1a)⁴. To understand the extent of

cortical vasculature that was contacted by pericytes that expressed low or undetectable α -SMA, that is, capillary pericytes, we immunostained 0.5–1-mm-thick coronal brain slices for α -SMA and optically cleared the tissue for imaging (Fig. 1b). The thick tissue sections preserved microvascular architecture and allowed us to assess α -SMA expression in mural cells along ~138 mm of total three-dimensional vascular length in sensory cortex. This revealed that the vast majority of vascular length (96 \pm 1% s.e.m.) was covered by mural cells with low or undetectable α -SMA, which are nearly all capillary pericytes, but also include a small number of cells on venules (Fig. 1c).

The expression level of α -SMA drops abruptly as precapillary arterioles transition into capillaries (Fig. 1d)^{4,5,12}. To ensure that our subsequent in vivo imaging experiments were targeting the capillary zone, we determined the maximum microvascular branch order at which α -SMA expression was detectable. This revealed that α -SMA expression decreased at or before the 4th branch order (Fig. 1e), a finding consistent with our past work and that of other groups using similar tissue fixation techniques^{5,12}. Thus, targeting microvessels of 5th branch order or greater during in vivo imaging studies ensures the examination of capillary pericytes. Figure 1f–h illustrates the central question of our study: Do capillary pericytes, which are morphologically⁴ and transcriptionally²⁰ distinct from upstream mural cells, influence local blood flow in vivo?

Concurrent blood flow imaging and two-photon optogenetic stimulation of capillary pericytes. To directly assess the contractile ability of capillary pericytes in vivo, we crossed PDGFR β -Cre mice

with reporter mice for the light-gated ion channel, ChR2-YFP (Fig. 2a and Supplementary Fig. 1a). To confirm that hemodynamic changes required ChR2 expression, and were not the result of non-specific effects of laser irradiation, we also bred PDGFR β -Cre mice with reporter mice for either cytosolic YFP or membrane-bound GFP (mT/mG) (Supplementary Fig. 1b,c). The mT/mG-expressing mice allowed us to further assess whether pericytes with membrane localization of fluorophore could respond to light differently than pericytes with a cytosolic fluorophore. Ultimately, we pooled the data from control mice into a single group, as no difference was observed between YFP and mT/mG groups (Supplementary Fig. 2).

In adult offspring from these crosses, we generated acute, skull-removed cranial windows over sensory cortex for two-photon imaging, and injected fluorescent dextran dye retro-orbitally to visualize the vasculature (intravenous (i.v.) dye; Texas red-dextran, 70 kDa) (Fig. 2a). Unless otherwise noted, experiments were conducted using light (0.8% minimum alveolar concentration (MAC)) isoflurane anesthesia delivered in air. Imaging of ChR2-YFP and mGFP revealed that capillary pericyte processes surrounded more of the endothelium than could be recognized from cytosolic YFP labeling (Supplementary Fig. 1g). This suggests a structural profile equipped to control capillary diameter.

Past studies indicate that the maximum two-photon activation of ChR2 occurs at ~900-nm excitation²¹. However, in practice we found that mere observation of arterioles and capillaries with 800-nm excitation was sufficient to induce vasoconstriction, whereas 900-nm excitation had little effect across a range of laser powers (Supplementary Fig. 3). This unexpected wavelength dependency for ChR2 activation in mural cells was also reported previously⁷. We leveraged the focal nature of this constrictive effect to probe the contractility of capillary pericytes independent from upstream mural cells. Navigation through the mouse brain was performed with low-power 900-nm excitation, and we switched to 800 nm for optogenetic activation once a target capillary pericyte was identified.

To concurrently activate ChR2-YFP and measure blood flow dynamics, we used multi-segmented line-scan paths that performed three functions (Fig. 2b). First, two-photon irradiation at 800 nm enabled spatially restricted pericyte stimulation near the laser focus, while avoiding coincident activation of upstream SMCs (Fig. 2c). Second, traversing the capillary lumen five times illuminated the i.v. dye, and provided multiple measurements of capillary diameter. Third, the line-scan bisected the central axis of the capillary lumen to track the movement of blood cells, from which we extracted the RBC flow velocity and RBC flux (blood cells per second). An *in vivo* example of this line-scan being applied to a capillary is shown in Fig. 2d, and the resulting space-time plot of the entire scan is provided in Fig. 2e with annotation of where lumen diameter and RBC flow metrics were collected (Supplementary Videos 1 and 2).

Capillary pericytes contract and reduce capillary flow in response to optogenetic activation. When we stimulated capillary pericytes (5th to 9th branch order) for 60 s with 800-nm line-scans, we observed a gradual decrease in capillary diameter in the ChR2-YFP group (~20% below baseline). This effect was most robust at laser powers in the range of 40–80 mW within the upper 100 μ m of cortex, although some constriction was also seen at lower powers (Supplementary Fig. 4). The constrictive effect was primarily mediated by ChR2-YFP activation, and not by the laser itself, because constriction was substantially smaller in controls (~5%) (Fig. 2f). Laser intensity as a function of cortical depth was well-matched between ChR2-YFP and control groups, eliminating the possibility that the groups received different levels of irradiation (Supplementary Fig. 5). Critically, vasoconstriction was associated with a decrease in RBC velocity and flux in the

same capillaries, showing that the induced levels of constriction were sufficient to alter blood flow (Fig. 2g–j). It also was confirmed that the diameter changes were not due to the capillary shifting from the imaging focal plane. This result was independent of anesthesia, as we obtained a similar outcome with animals lightly sedated by chlorprothixene instead of isoflurane (Supplementary Fig. 6a,b).

Our data support the idea that capillary flow reduction was due to locally induced pericyte contraction, as opposed to a passive downstream deflation that might occur if stimulation had been conducted upstream to constrict arterioles²². Capillary diameter deviated from baseline earlier than did RBC velocity, that is, within 10 s for lumen diameter (Fig. 2f) versus 30 s for RBC velocity (Fig. 2g). If upstream arteriole constriction had triggered a downstream deflation of capillaries, one would instead expect RBC velocity change to precede diameter change.

During stimulation with line-scans, we observed complete cessation of blood flow in 12% of capillaries from ChR2-YFP mice, but none from control mice. To better understand the persistence of these flow stalls, we also collected full-field image stacks at 900 nm 1–3 min after the 60-s stimulation period for all vessels imaged. We observed sustained stalling of RBCs in ~30% of capillaries from ChR2-YFP mice, but in only 3% of capillaries from control mice (Supplementary Fig. 7). Stalled capillaries had smaller diameter and lower RBC velocity and flux at baseline (Supplementary Fig. 8a–c). Capillaries with flow stalls were not appreciably different with respect to branch order from the penetrating arteriole (Supplementary Fig. 8d). Collectively, these data indicate that capillary pericytes are able to constrict capillaries and maintain contraction over a protracted time-scale.

We further examined whether contractility occurred preferentially at the pericyte soma, by dividing the ChR2-YFP dataset into two groups, ‘soma’ or ‘no soma’, based on whether any portion of the multi-segment line-scan transected the pericyte soma (Supplementary Fig. 9a,b). Soma location could be discerned from full-field image stacks collected before and after each line-scan. These two groups showed no detectable difference in decrease of capillary diameter, RBC velocity or RBC flux (Supplementary Fig. 9c–e), indicating that capillary pericytes can exert force at both their somata and processes. Considering that most of the endothelial contact made by capillary pericytes is through their extensive processes, this suggests a broad impact on capillary flow by pericytes.

In 30% of optogenetically stimulated capillary pericytes, we observed localized blebbing (small membrane protrusions) along the pericyte wall, likely due to disruption of the actin cytoskeleton caused by contraction to supra-physiological levels (Supplementary Fig. 10a–e). These local protrusions were reminiscent of blebs described during pericyte contraction in response to endothelin-1 (ref. 23). Blebbing was not the result of photo-damage because it was not observed in control mice. It also did not drive the genotype effects on capillary hemodynamics, as omitting blebbed cells from the dataset had no effect on statistical significance of capillary flow reduction in ChR2-YFP mice (Supplementary Fig. 10f,g).

Fasudil blocks optogenetically induced capillary constriction. We next asked whether optogenetic contraction of capillary pericytes relied upon cellular contractile machinery. In SMCs, Rho-kinase inhibits myosin light chain phosphatase to promote myosin light chain phosphorylation and vasoconstriction through actomyosin cross-bridging. The Rho-kinase inhibitor fasudil inhibits this pathway and promotes vasodilation. In addition, fasudil also inhibits SMC contraction by blocking polymerization of cytoskeletal actins. Fasudil does not alter conductance of L-type calcium channels in mural cells²⁴, which mediates mural cell membrane voltage changes induced by ChR2 activation²⁵.

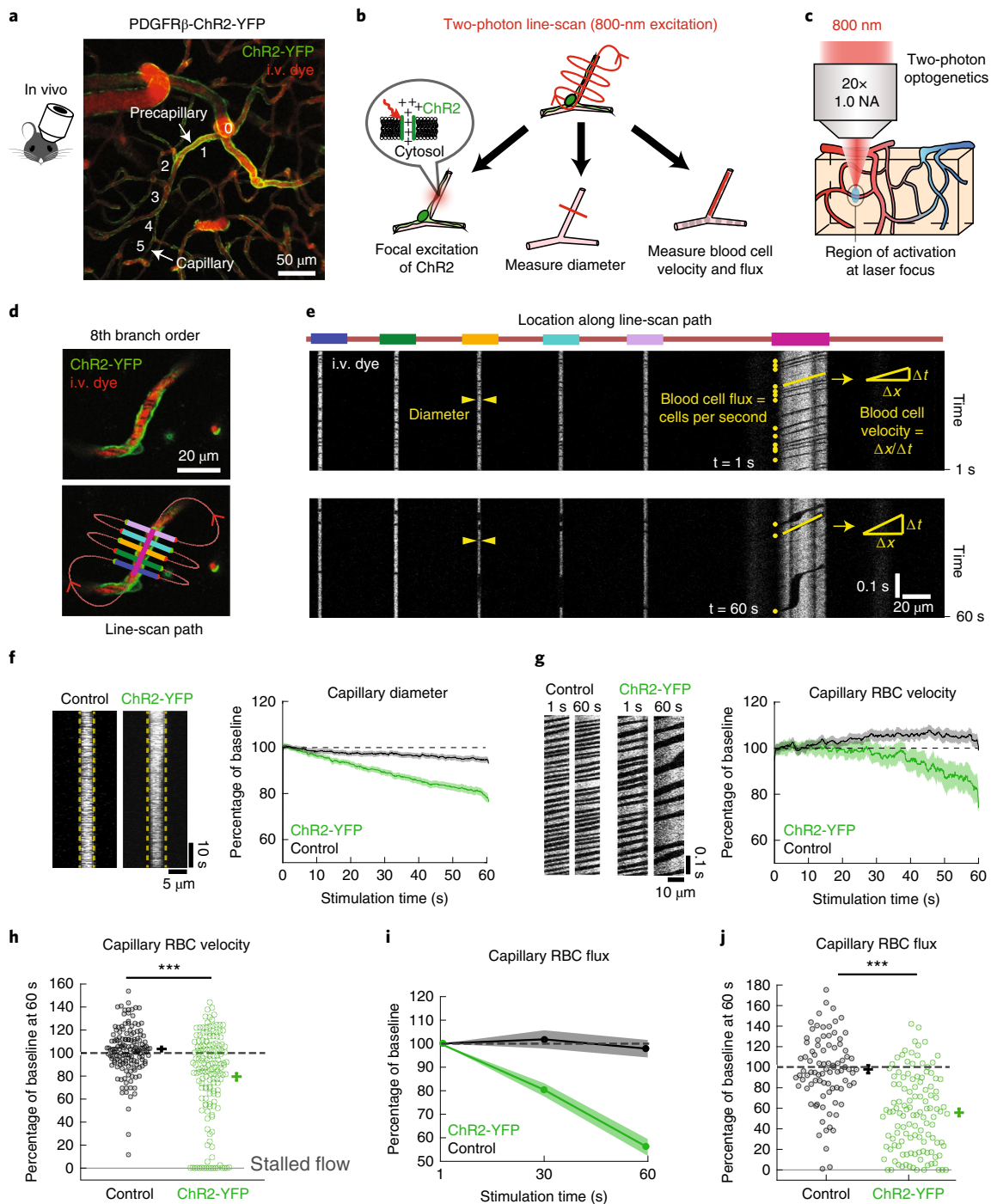


Fig. 2 | Optogenetic activation of capillary pericytes constricts capillaries and reduces blood flow. a, In vivo two-photon image from PDGFR β -ChR2-YFP mouse with microvascular branch orders. **b**, Two-photon line-scans (red) used to simultaneously stimulate ChR2-YFP and measure capillary vasodynamics. **c**, Two-photon excitation of ChR2-YFP allows focal activation of pericytes below the brain surface. **d**, Example of capillary pericyte in ChR2-YFP mouse with line-scan path. Colored segments correspond to the same-colored regions at the top of **e**. **e**, Line-scan data resulting from repeatedly scanning the path shown in **d**. Upper image shows beginning of line-scan, and lower image shows the end of a continuous 60-s scan. **f**, Left: example of diameter portion of line-scan over 60 s of stimulation, comparing YFP control and ChR2-YFP. Dotted yellow lines demarcate diameter at baseline. Right: time-course of diameter change during stimulation of capillaries. ChR2-YFP: $n = 155$ capillaries (10 mice); controls: $n = 145$ capillaries (9 mice). **g**, Left: example of blood flow portion of line-scan. Right: time-course for RBC velocity change during stimulation of capillaries. ChR2-YFP: $n = 160$ capillaries (10 mice); controls: $n = 152$ capillaries (9 mice). **h**, Change in RBC velocity at 60 s relative to baseline. $F(1, 290) = 26.8$, $***P < 0.0001$, one-way repeated-measures ANOVA (two-tailed). ChR2-YFP: $n = 157$ capillaries (10 mice); controls: $n = 152$ capillaries (9 mice). **i**, Time-course of RBC flux change during stimulation of capillaries. **j**, Change in RBC flux at 60 s relative to baseline. $F(1, 186) = 42.48$, $***P < 0.0001$ by one-way repeated-measures ANOVA (two-tailed). ChR2-YFP: $n = 118$ capillaries (10 mice); controls: $n = 87$ (9 mice) capillaries. All time-course and scatter plots in this figure show mean \pm s.e.m.

Fasudil was incorporated into an agarose layer overlying the cortical surface during preparation of an acute cranial window, with concentrations 10-fold (1 mM) and 100-fold (10 mM) higher than a commonly used *ex vivo* concentration. This allowed for direct access to the brain and accounted for drug dilution as it crossed the meninges and entered the brain interstitial fluid. Under basal conditions, fasudil caused dilation of pial arterioles and capillaries, but without effects on capillary RBC velocity (Supplementary Fig. 11). However, fasudil increased baseline capillary RBC flux, by packing RBCs more tightly (Supplementary Fig. 12). During optogenetic stimulation of capillary pericytes, fasudil attenuated relative and absolute capillary constriction in a dose-dependent manner (Fig. 3a and Supplementary Fig. 11e,f). Further, reduction of RBC velocity and flux was also prevented (Fig. 3b,c). Accordingly, blockade of constriction also led to a dose-dependent alleviation of persistent flow stalls (Supplementary Fig. 13). The incidence of pericyte blebbing was also markedly reduced, in line with the idea that the membrane protrusions were a Rho-kinase-dependent process involving actin cytoskeleton reorganization (Supplementary Fig. 14). Collectively, these data support the idea that optogenetic stimulation of capillary pericytes engages cellular contractile machinery that can be pharmacologically modulated.

Reactive oxygen species (ROS) may link Chr2 activation and mural cell contraction. Given the unexpected dependencies on laser power and wavelength for optogenetically induced vasoconstriction (Supplementary Figs. 3 and 4), we asked whether ion flux through Chr2 acted together with other processes to engage contractile machinery. We focused on ROS because mural cell calcium influx can produce ROS via mitochondrial calcium uptake²⁶, and ROS are known to cause vasoconstriction by activating Rho-kinase²⁷. Further, previous studies seeking to optically stimulate SMCs found that much higher levels of 800-nm light (>300 mW) could elevate intracellular calcium through a process inhibited by antioxidants, such as N-acetyl cysteine (NAC)²⁸. We therefore added 100 mM NAC to the agarose layer above the cortical surface. Vasoconstriction in pre-capillary arterioles and capillaries of Chr2 mice was abrogated by NAC treatment (Supplementary Fig. 15a,b,d,e). This was not because vessels were already constricted by NAC, as baseline diameter was unaffected (Supplementary Fig. 15c,f). These data suggest that Chr2 activation and 800-nm light work synergistically to generate ROS, which in turn drives contractile machinery-dependent vasoconstriction.

Capillary pericytes constrict more slowly than upstream mural cells with high α -SMA content. We next compared the contractile dynamics of capillary pericytes against mural cells of other microvascular zones by applying a similar line-scan pattern to other vessel types (Fig. 4a–d). We found that stimulation of pial arteriole SMCs in Chr2-YFP mice led to a more robust and rapid vasoconstriction than seen in capillary pericytes. A maximal arteriolar constriction of 40% was induced within the first 25 s of stimulation, followed by gradual relaxation back to baseline despite continued stimulation (Fig. 4a). Stimulation of pial arterioles in control animals exhibited a smaller and slower change, reaching only 15% constriction by the end of the 60-s stimulation period, confirming that the rapid constriction response was Chr2-dependent (Fig. 4a). No significant diameter change was observed with stimulation of mural cells on pial venules in either Chr2-YFP or control animals (Fig. 4d,e).

Below the pial surface, ensheathing pericytes and capillary pericytes contracted when Chr2 was stimulated, but were both slower relative to SMCs of pial arterioles (Fig. 4b,c,e). When comparing relative diameter change after 60 s of stimulation, there was no significant difference between the cell types (Fig. 4e), despite clear

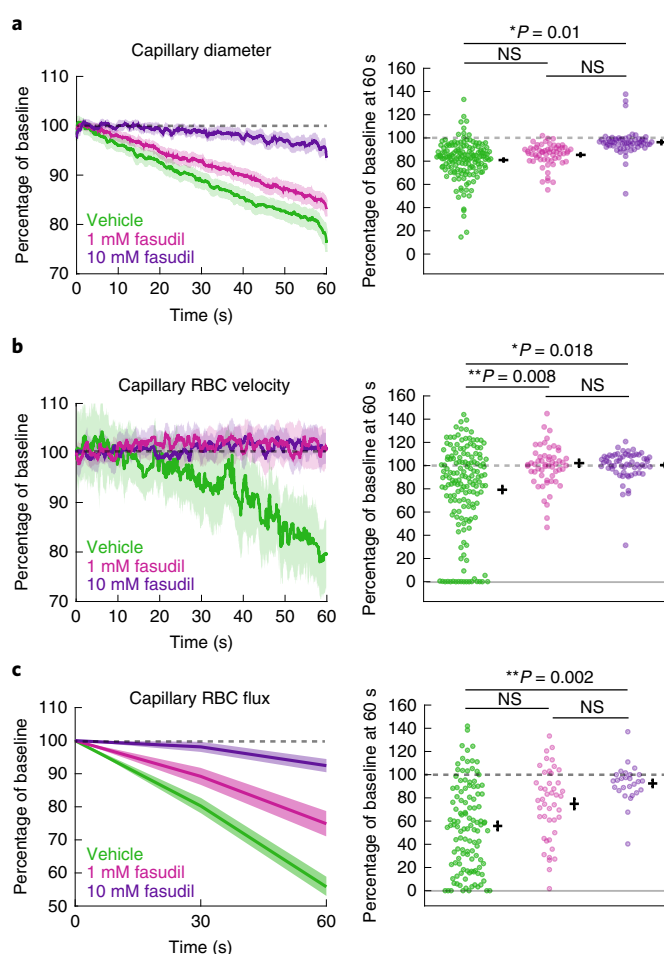


Fig. 3 | Topical administration of fasudil prevents hemodynamic changes induced by optogenetic stimulation of capillary pericytes. **a–c**, Left: fasudil inhibits reduction in capillary diameter (**a**), RBC velocity (**b**) and RBC flux (**c**) during optogenetic stimulation of capillary pericytes in Chr2-YFP mice. Right: change in diameter (**a**), RBC velocity (**b**) and RBC flux (**c**) at 60 s of stimulation relative to baseline. *P* values are from one-way repeated-measures ANOVA (two-tailed) adjusted by Tukey post hoc test (overall ANOVA test, $P < 0.015$ for **a–c**; $F(2, 174) = 6.63$, for **c**; other panels had higher *F* values). **a**, Capillary diameter: $P = 0.7146$ (vehicle versus 1 mM fasudil), $*P = 0.0098$ (vehicle versus 10 mM fasudil), $P = 0.1855$ (1 mM fasudil versus 10 mM fasudil). Vehicle: $n = 154$ (10 mice); 1 mM fasudil: $n = 60$ (3 mice); 10 mM fasudil: $n = 60$ (3 mice). **b**, RBC velocity: $**P = 0.008$ (vehicle versus 1 mM fasudil), $*P = 0.0181$ (vehicle versus 10 mM fasudil), $P = 0.9679$ (1 mM fasudil versus 10 mM fasudil). Vehicle: $n = 157$ (10 mice); 1 mM fasudil: $n = 57$ (3 mice); 10 mM fasudil: $n = 61$ (3 mice). **c**, RBC flux: $P = 0.118$ (vehicle versus 1 mM fasudil), $**P = 0.0021$ (vehicle versus 10 mM fasudil), $P = 0.3654$ (1 mM fasudil versus 10 mM fasudil). Vehicle: $n = 118$ (10 mice); 1 mM fasudil: $n = 45$ (3 mice); 10 mM fasudil: $n = 27$ (3 mice). All time-course and scatter plots show mean \pm s.e.m. NS, not significant.

differences in α -SMA content (Fig. 1g,h). However, since pre-capillary arterioles were slightly larger than capillaries at baseline (Fig. 4f), we also compared rate changes in absolute vessel diameter. This revealed that stimulation of ensheathing pericytes produced ~ 2.6 -fold-faster initial contractions than did similar activation of capillary pericytes (Fig. 4g,h).

Next we examined capillary responses as a function of branch order within the capillary group. This revealed similar magnitudes

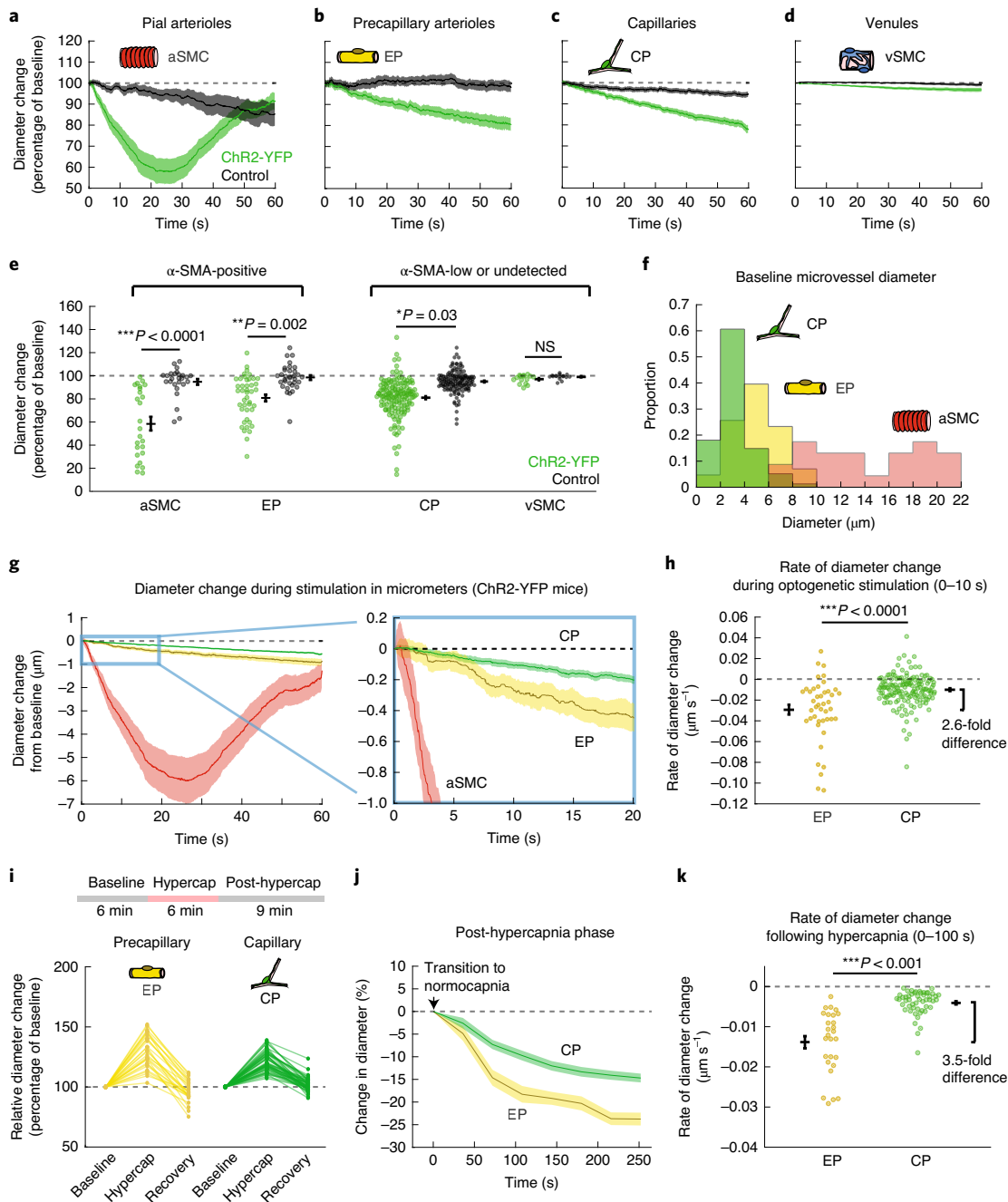


Fig. 4 | Distinct contractile dynamics of mural cells in different microvascular zones. **a–d**, Change in diameter during optogenetic stimulation of mural cells in different microvascular zones. Pial arterioles (**a**): $n = 25$ (5 ChR2-YFP mice), $n = 26$ (4 control mice); precapillary arterioles (**b**): $n = 43$ (10 ChR2-YFP mice), $n = 33$ (9 control mice); capillaries (**c**): $n = 155$ (10 ChR2-YFP mice), 145 (9 control mice); venules (**d**): $n = 15$ (4 ChR2-YFP mice), $n = 16$ (3 control mice). **e**, Diameter change from baseline at 60 s of stimulation (25 s for arteriole SMCs). For ChR2 vessel type (statistics not shown on graph): $F(3, 429) = 16.51$, overall effect $***P < 0.0001$; $***P < 0.0001$ aSMC versus EP, $***P < 0.0001$ aSMC versus CP, $***P < 0.0001$ aSMC versus vSMC, $P = 0.66$ EP versus CP, $**P = 0.007$ EP versus vSMC, $*P = 0.029$ CP versus vSMC. For genotype (ChR2 versus control): $F(1, 429) = 21.53$, overall effect $***P < 0.0001$, $***P < 0.0001$ for aSMC, $**P = 0.0017$ for EP, $*P = 0.029$ for CP, $P = 0.9986$ for vSMC. For interaction between vessel type and genotype: $F(3, 429) = 11.92$, $***P < 0.0001$. Two-way repeated-measures ANOVA (two-tailed). Tukey post hoc analyses were used to compare between vessel types or genotypes. All n values as in **a**. **f**, Histogram showing distribution of baseline diameters for different vessel types. Pial arterioles: $n = 155$ (10 mice); precapillary arterioles: $n = 43$ (10 mice); capillaries: $n = 25$ (5 mice). **g**, Left: absolute diameter change from baseline for capillaries (green), precapillary arterioles (yellow) and arterioles (red) during optogenetic stimulation of vessels in ChR2-YFP mice. Right: magnified view of differences in early constriction phase. **h**, Rate of diameter change during first 10 s of optogenetic stimulation of precapillary arterioles and capillaries. $F(1, 186) = 37.86$, $***P < 0.0001$, one-way repeated-measures ANOVA (two-tailed). Precapillary arterioles: $n = 43$ (9 mice); capillaries: $n = 155$ (10 mice). **i**, Top: experimental time-course for hypercapnia studies. Bottom: change in precapillary arteriole and capillary diameters at the end of the hypercapnic phase (hypercap), and 9 min after return to normocapnia (recovery). Precapillary: $n = 27$ (5 mice); capillary: $n = 51$ (5 mice). **j**, Time-course of vessel diameter change following transition from hypercapnia to normocapnia. Same n values as in **i**. **k**, Rate of diameter change after hypercapnia. $***P < 0.001$, linear mixed-effects modeling (two-tailed). Same n values as in **i**. All time-course data and scatter plots in this figure show mean \pm s.e.m. aSMC, arteriole SMC; CP, capillary pericyte; EP, ensheathing pericyte; vSMC, venule SMC.

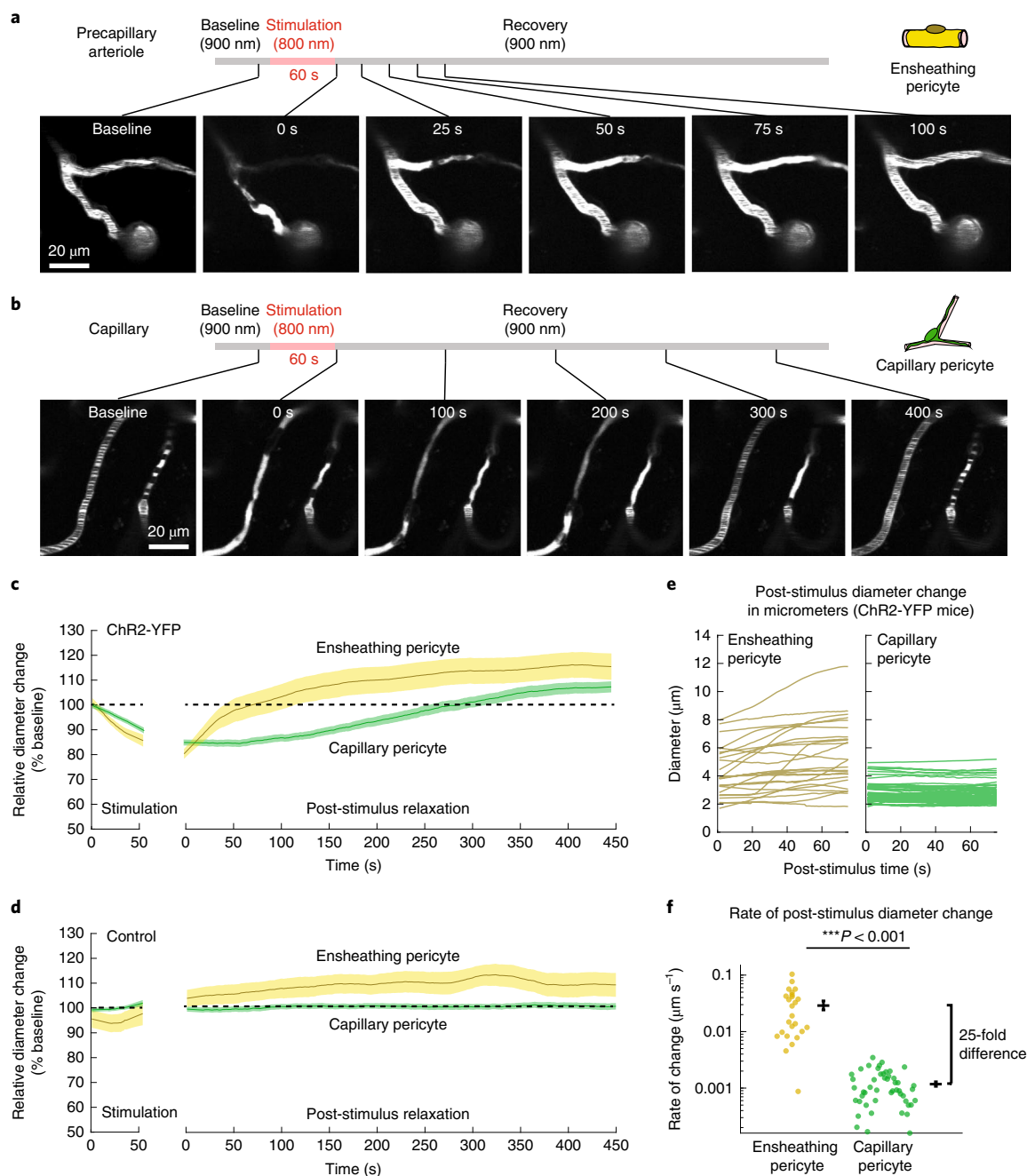


Fig. 5 | Dilation after optogenetic vasoconstriction is faster in precapillary arterioles than capillaries. a,b, Example of vessel constriction followed by post-stimulus relaxation with optogenetic stimulation of ensheathing pericytes (**a**) versus capillary pericytes (**b**). **c,d**, Time-course of change in precapillary arteriole and capillary diameters during and after optogenetic stimulation in PDGFR β -ChR2-YFP mice (**c**) and PDGFR β -YFP controls (**d**). PDGFR β -ChR2-YFP: ensheathing pericyte: $n=20$ (6 mice); capillary pericyte: $n=49$ (6 mice). PDGFR β -YFP (control): ensheathing pericyte: $n=13$ (3 mice); capillary pericyte: $n=61$ (3 mice). **e**, Change in absolute vessel diameter in the first 80 s of post-stimulus relaxation for PDGFR β -ChR2-YFP mice. Same n values as in **c, f**. **f**, Rate of diameter change after optogenetic stimulation. $F(72)=197.73$, $***P < 0.001$ by linear mixed-effects modeling (two-tailed). Ensheathing pericyte: $n=20$ (6 mice); capillary pericyte: $n=49$ (6 mice). All time-course and scatter plots in this figure show mean \pm s.e.m.

of constriction and reduction in RBC flow among all branch orders (Supplementary Fig. 16a–d). Because earlier studies in retina have shown α -SMA expression up to the 7th branch order using special fixation techniques, we subgrouped these data for statistical analysis and found no difference between responses in 5th to 7th order capillaries versus 8th to 9th order capillaries (Supplementary Fig. 16e–g), suggesting that capillary constriction can occur beyond regions with known α -SMA expression.

Average constriction appeared nearly linear through the 60-s stimulation period for precapillary arterioles and capillaries (Fig. 4b,c). However, a subset of vessels had reached a maximum constriction before the end of the scan, as evident from a plateau in diameter (Supplementary Fig. 17a–d). Capillaries that plateaued did not differ from those that continued to constrict in any vasodynamic metric examined (Supplementary Fig. 17e–g). We calculated the time to half-maximum constriction for all

vascular zones, and observed a graded increase from arterioles to precapillary arterioles to capillaries (Supplementary Fig. 18a–d). As expected, the contraction magnitude exhibited a graded decrease across the same microvascular zones (Supplementary Fig. 18e). Collectively, these data indicate that capillary pericytes can contract *in vivo*, but with slower dynamics than upstream α -SMA-expressing mural cells.

Capillaries are slower to contract back to baseline following hypercapnic dilation. To investigate the constrictive rate of microvessels in a more physiologic context, we measured the diameter of precapillary arterioles and capillaries following transient hypercapnic challenge (5% CO₂ in air for 6 min). Hypercapnia induced robust and reliable dilation of both capillaries and precapillary arterioles, and constriction to baseline occurred upon reinstatement of normocapnia (Fig. 4i, Supplementary Fig. 19 and Supplementary Video 3)^{29,30}. The rate of constriction to baseline after hypercapnia was significantly slower in capillaries than in precapillary arterioles, particularly in the first 100 s after transition to normocapnia (Fig. 4j,k). The difference in constrictive rate between these microvascular zones was comparable for optogenetic stimulation and recovery after hypercapnia. That is, precapillary arterioles constricted ~2.5-fold and 3.5-fold faster than capillaries during ChR2 activation and after hypercapnia, respectively (Fig. 4h,k). Thus, interpreted alongside the cause-and-effect optogenetic studies, contractile kinetics differed between ensheathing pericytes and capillary pericytes during physiologically relevant blood flow modulation.

Precapillary arterioles dilate over seconds, but capillaries dilate over minutes when recovering from vasoconstriction. Intravascular pressure competes against vasoconstriction, but facilitates the process of vasodilation. The kinetics of dilation may therefore be quite distinct from constriction. To further investigate this idea, we imaged the relaxation of precapillary arterioles and capillaries following optogenetically induced constriction. We used two-dimensional video scans instead of line-scans to gain a better view of the constrictive and dilatory dynamics. Capillary fields contained no precapillary arterioles to ensure no indirect influence of upstream flow. After 60 s of optogenetic stimulation, we then switched to imaging with 900-nm excitation. Precapillary arterioles exhibited rapid dilation, returning to baseline within 50 s, on average, and ultimately settling just above baseline diameters (Fig. 5a,c,e). In some cases when maximal constriction had been achieved in precapillary arterioles, the lumen opened first proximal to the penetrating arteriole and then gradually more distal along the vessel length, consistent with influence of upstream intravascular pressure (Fig. 5a and Supplementary Videos 4 and 5). In one instance, we observed a persistent ‘sphincter-like’ constriction in a distal region of the precapillary arteriole, despite rapid dilation

upstream (Supplementary Video 5). In contrast, all capillaries examined dilated considerably slower, requiring on average ~300 s to regain baseline levels (Fig. 5b,c,e and Supplementary Videos 6 and 7). This corresponded to a 25-fold-faster rate of dilation in precapillary arterioles, compared with capillaries (Fig. 5f). Control mice expressing only YFP showed no vasoconstriction during imaging with 800-nm excitation (Fig. 5d and Supplementary Videos 8 and 9). Prolonged scanning of ensheathing pericytes in YFP mice led to a slight vasodilation of precapillary arterioles, suggesting that part of the dilatory response in ChR2-YFP mice was driven by light itself. However, the laser light had no effect on capillary diameter in YFP mice.

Thus, relaxation of ensheathing pericytes combined with high intravascular pressure at the precapillary arteriole enables rapid vasodilation, which is not observed at the capillary level. This result is in line with recent studies showing that ensheathing pericytes are an early and robust responder to vasoactive stimuli and neural activity^{8,10,11,31}.

Selective optical ablation of capillary pericytes increases capillary flow. Having established that contraction of capillary pericytes is sufficient to reduce blood flow on a slow time-scale, we hypothesized that a physiological role is to maintain enduring basal capillary tone and blood flow resistance. To test this, we used two-photon optical ablation to eliminate individual pericytes, as described previously³². In this procedure, precise line-scans with a shorter wavelength (725 nm) and higher power were used to specifically irradiate the somata of pericytes protruding from the capillary wall, killing the cell through photo- and thermal toxicity (Fig. 6a). Death of the targeted pericyte was confirmed by immediate loss of cellular fluorescence, which persisted in the days following the ablation. As a control for the effects of laser irradiation, we included a sham irradiation control where line-scans of equivalent laser power were placed with similar proximity to the capillary wall but not on a pericyte soma (Fig. 6b).

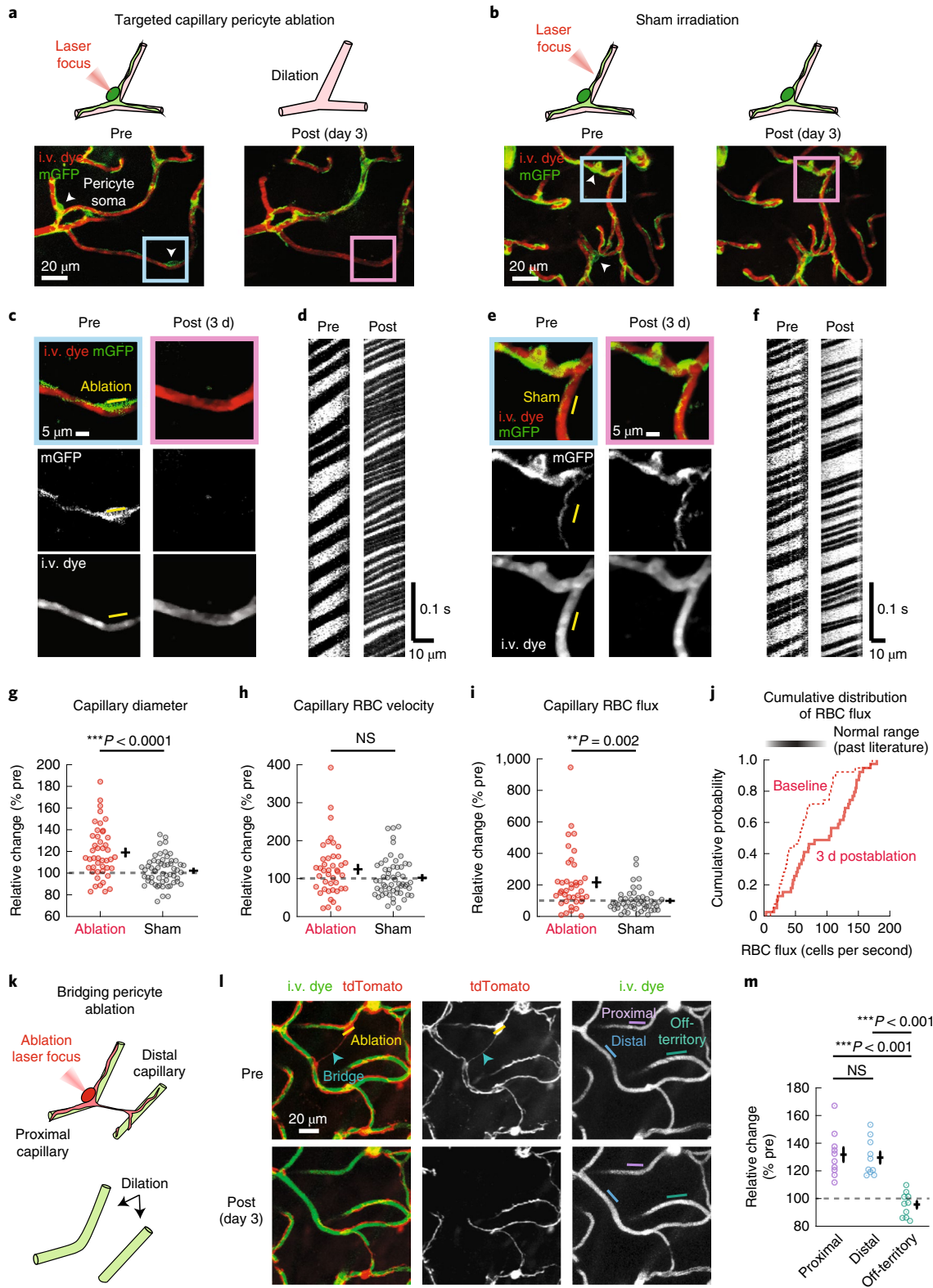
When capillary diameter was re-examined 3 d after pericyte ablation, we observed sustained dilation averaging ~20% over baseline, with some vessels showing up to 60–80% dilation, which corresponds to a ~2- μ m increase in absolute diameter (Fig. 6c,g). While this local dilation was not associated with a significant increase in RBC velocity (Fig. 6d,h), it produced a twofold increase of RBC flux compared with the sham group (Fig. 6d,i), as predicted by recent capillary flow modeling studies³³. In contrast, we found no change in diameter, RBC velocity or RBC flux over time for the sham irradiation group (Fig. 6e–i). The postablation flux values exceeded the RBC flux ranges found in previous studies of normal isoflurane-anesthetized mouse cortex^{34,35}. For instance, a recent study found that only ~10% of capillaries exceeded RBC flux rates of 100 cell per second (ref. ³⁵). In contrast, ~50% of capillaries

Fig. 6 | Ablation of individual capillary pericytes produces local capillary dilation and increased RBC flux. **a**, Before and 3 d after ablation of two capillary pericytes (arrowheads) in a PDGFR β -mT/mG mouse. **b**, Sham controls involve identical scan parameters as for cell ablation, but with the laser focus away from the pericyte somata. **c**, Magnified image of the boxed region in **a**, showing precise location of laser irradiation (yellow line). **d**, Line-scans for assessment of capillary vasodynamics in the adjoined capillary segment before and after pericyte ablation. **e, f**, Magnified image of boxed region in **b** (**e**) and corresponding line-scan data (**f**). **g–i**, Fold-change in capillary diameter (**g**), RBC velocity (**h**), and RBC flux (**i**) 3 d following pericyte ablation or sham irradiation. For **g**, $F(1,95) = 21.46$, $***P < 0.0001$ by one-way repeated-measures ANOVA (two-tailed); ablation: $n = 45$ capillaries (6 mice); sham: $n = 57$ capillaries (6 mice). For **h**, $F(1,88) = 1.3$, $P = 0.26$ by one-way repeated-measures ANOVA (two-tailed); ablation: $n = 41$ capillaries (6 mice); sham: $n = 54$ capillaries (6 mice). For **i**, $F(1,81) = 9.79$, $**P = 0.002$ by one-way repeated-measures ANOVA (two-tailed); ablation: $n = 39$ capillaries (6 mice); sham: $n = 49$ capillaries (6 mice). **j**, Cumulative distribution plot of RBC flux at baseline and 3 d postablation. A normal range for capillary RBC flux based on past literature is provided for comparison (see text for references). $N = 42$ capillaries (6 mice). **k**, Schematic showing the ablation of a bridging pericyte. **l**, Top: a bridging pericyte targeted for ablation (yellow line across soma) with process reaching across the parenchyma to contact a distant vessel (arrowhead). Bottom: after ablation, pericyte contact is lost on two vessels, proximal and distal to the ablated soma. **m**, Change in capillary diameter as a consequence of bridging pericyte ablation. ‘Off-territory’ is a neighboring capillary that retains pericyte coverage. $P = 0.9501$ (proximal versus distal), $***P = 0.002$ (proximal versus off-territory), $***P = 0.0007$ (distal versus off-territory); Kruskal-Wallis test: $X^2(2) = 19.45$ overall, with adjusted P values shown after Tukey post hoc test. $N = 10$ bridging pericyte ablations (7 mice).

exceeded flux of 100 cells per second after pericyte loss, indicating that abnormally high rates of RBC flux were induced (Fig. 6j).

To further ensure that the observed dilations were not the result of unintended damage to surrounding neurovascular structures (astrocyte endfeet, endothelium), we ablated ‘bridging’ pericytes that extended their processes across the parenchyma to contact territory on distant capillary segments (Fig. 6k–m and Supplementary

Fig. 20a). These pericyte ‘bridges’ are thought to be remnants of developmental vascular pruning and similar structures in the retina may be important for neurovascular coupling³⁶. We observed dilation of uncovered capillary segments adjacent to the ablated pericyte soma (‘proximal’ segment), as well as segments contacted by the pericyte bridge distant from the site of irradiation (‘distal’ segment). Importantly, nearby segments still in contact with other



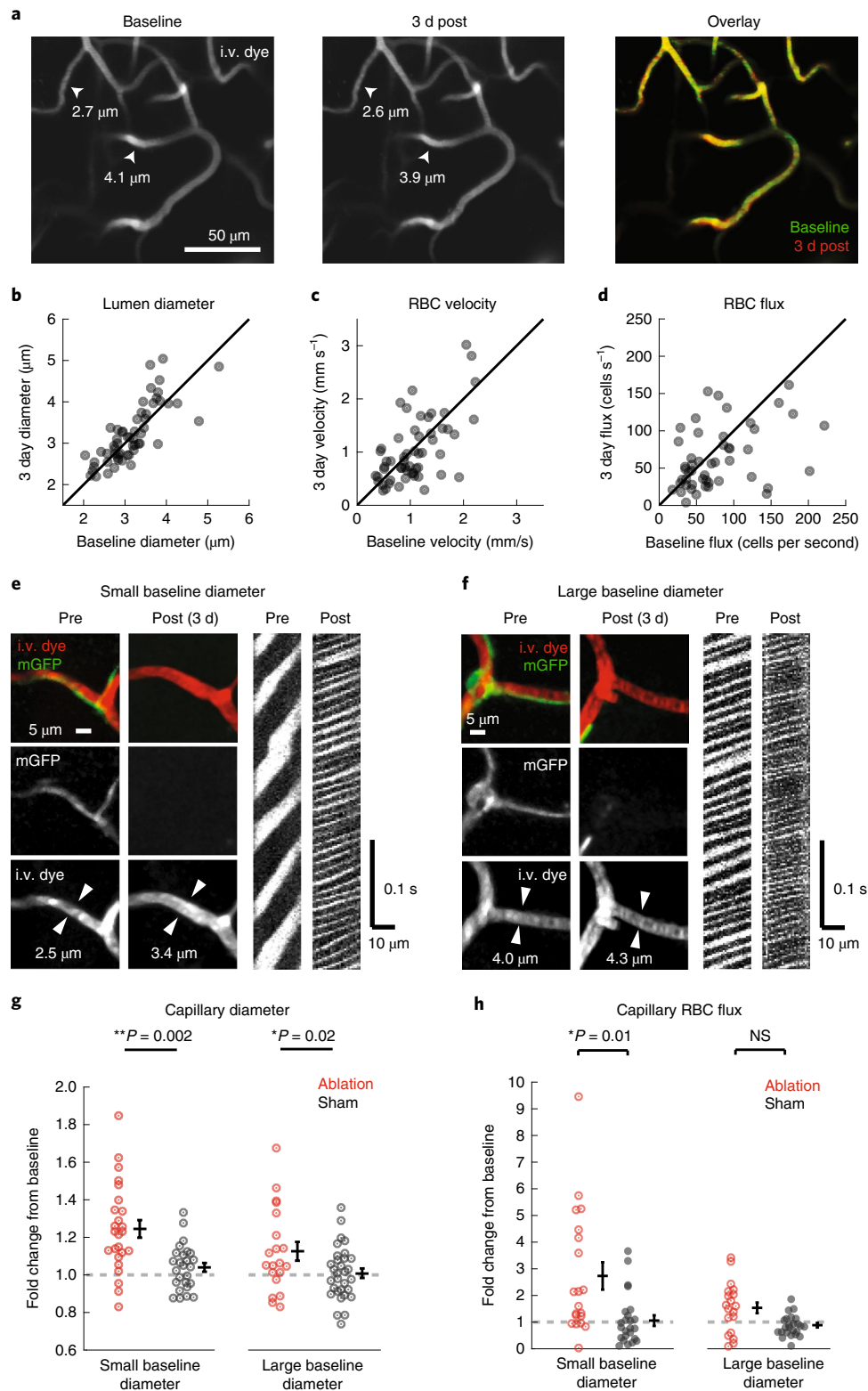


Fig. 7 | Pericytes control heterogeneity of basal capillary vasodynamics. **a**, Images of i.v. dye channel collected 3 d apart from the same cortical region. One small-diameter capillary and one larger-diameter capillary are highlighted. **b–d**, Scatter plots of capillary vasodynamic parameters collected at baseline versus 3 d. Pearson's correlation: lumen diameter (**b**): $R^2 = 0.62$, $***P < 0.001$; $n = 57$ capillaries (6 mice); RBC velocity (**c**): $R^2 = 0.39$, $***P < 0.001$; $n = 56$ capillaries (6 mice); and RBC flux (**d**): $R^2 = 0.17$, $***P < 0.01$; $n = 49$ capillaries (6 mice). **e, f**, Example images and line-scan data collected before and 3 d following capillary pericyte ablation. A small-baseline-diameter capillary (**e**) and a large-baseline-diameter capillary (**f**) are shown. **g, h**, Fold-change in capillary diameter (**g**) and RBC flux (**h**) in small- and large-diameter capillaries after pericyte ablation. For **g**, small baseline diameter: $F(1,44) = 11.51$, $***P = 0.0015$; ablation: $n = 25$ (6 mice), sham: $n = 26$ (6 mice); large baseline diameter: $F(1,44) = 6.28$, $*P = 0.016$; ablation: $n = 20$ (6 mice), sham: $n = 31$ (6 mice), by repeated-measures ANOVA (two-tailed). For **h**, small baseline diameter: $F(1,42) = 6.83$, $*P = 0.0124$; ablation: $n = 24$ (6 mice), sham: $n = 25$ (6 mice); large baseline diameter: $P = 0.14$; ablation: $n = 15$ (6 mice), sham: $n = 24$ (6 mice) by one-way repeated-measures ANOVA (two-tailed). All data are shown as mean \pm s.e.m.

pericytes did not change in diameter ('off-territory' segment) (Fig. 6l,m and Supplementary Fig. 20b). In some cases, bridging pericyte somata were located within the parenchyma, tethered between two primary processes that extended to contact two capillaries (floating pericyte). Ablation of these pericytes also led to dilation of both capillaries contacted by the processes of the ablated cell (Supplementary Fig. 20c). These data show that loss of pericyte–endothelial contact is the basis of capillary dilation, and that damage to other cells is unlikely to be involved.

Within minutes postablation, small but consistent capillary dilations could be detected, suggesting immediate loss of capillary tone as opposed to long-term endothelial remodeling (Supplementary Fig. 21). In the chronic time-frame, neighboring pericytes extended their processes to re-cover the exposed endothelium, allowing capillaries to regain their normal diameter, consistent with our previous studies (Supplementary Fig. 22)³². Collectively, these data support the idea that capillary pericytes actively maintain flow resistance throughout the capillary network, and that loss of pericytes leads to local capillary dilation and augmentation of RBC flux.

Greater dilation of capillaries with smaller baseline diameter after pericyte ablation. Under basal conditions, brain capillaries are heterogeneous in diameter and flow rate. This heterogeneity is thought to create a blood flow 'reserve' by providing room for the homogenization of flow across the capillary bed during functional hyperemia^{35,37–39}. Consistent with this idea, we observed that capillary diameter and blood cell flux were highly heterogeneous even within small volumes of tissue (Fig. 7a–d), and diameter was quite stable over 3 d (Fig. 7b–d). To better understand the origins of this heterogeneity, we asked whether capillary diameter influenced blood flow at baseline. Indeed, we found a weak but significant positive correlation between capillary diameter and RBC velocity and flux, in line with a previous study (Supplementary Fig. 23a,b)⁴⁰.

If pericytes were involved in creating capillary flow heterogeneity, one would expect that some vessels are narrow because pericytes are consistently exerting more tone on them, and other vessels are dilated because their associated pericytes are relatively relaxed. In line with this idea, we found that ablation of pericytes on small-diameter capillaries produced greater dilations than did ablation of pericytes on larger-diameter capillaries (Fig. 7e,f and Supplementary Fig. 23c). We further split our dataset at the median diameter of 3 μm to compare 'small' versus 'large' baseline diameter groups (Fig. 7g,h and Supplementary Fig. 23e). Small and large capillaries both dilated significantly after ablation when compared with sham, but small-diameter capillaries dilated twofold more (~24% dilation) than large-diameter capillaries (~12% dilation) (Fig. 7g). Further, only the small capillary group showed a significant increase in RBC flux compared with the sham group (Fig. 7h and Supplementary Fig. 23d). Together, these data suggest that pericytes throughout the capillary bed exert variable levels of tone, which contributes to enduring capillary flow heterogeneity under basal conditions.

Discussion

Capillary pericytes contact more than 90% of the total vascular length in the cerebral cortex, yet their ability to regulate blood flow in vivo has remained elusive. Using cause-and-effect optical manipulations in vivo, we show that capillary pericytes can modulate capillary diameter and influence blood flow (Supplementary Fig. 24). However, this control over capillary diameter occurs with slower kinetics than for upstream α -SMA-positive mural cells. The slow contractility of capillary pericytes suggests a role in establishing basal capillary flow resistance and heterogeneity at rest, and opens the possibility that capillary pericytes modulate late phases of functional hyperemia or even slower physiologic phenomena. This is in contrast to the rapid kinetics required for the initial phases of

neurovascular coupling, which appears to be a role better played by upstream precapillary arterioles^{5,8,41,42}.

A past study by Hill et al. used a similar optogenetic approach, and concluded that capillary pericytes could not constrict capillaries⁵. However, this study may have overlooked their contractile ability by examining shorter periods of stimulation relevant to neurovascular coupling (up to 20 s). The laser powers used for optogenetic stimulation may also have been below the threshold needed to discern capillary pericyte contraction. In support of our findings, a recent single-photon optogenetic study by Nelson et al. also reported that brain capillary pericytes are contractile, but function on a slow time-scale⁴³. With respect to contractile machinery, transcriptomic studies indicate that capillary pericytes express nearly all components needed for actomyosin-based contraction, including myosin (*myh11*, *myl9*, *myh9*), regulators of myosin phosphorylation state (*mylk* and *Ppp1r12b*, *ROCK1*) and L-type voltage-gated calcium channels (*cacna1c*)²⁰. However, little to no smooth muscle actin expression (*acta1*, *acta2*, *actg2*, *actc1*) is detected, making the binding partner of the myosin proteins unclear. In retina, recent studies have shown that α -SMA and F-actin polymerization is involved in contraction of capillary pericytes^{44,45} and that immunohistochemical detection of low-level α -SMA requires specialized fixation procedures⁴⁶. Therefore, it is possible that *acta2*/ α -SMA expression is simply low and difficult to detect in capillary pericytes, yet sufficient in quantity to support slow actomyosin contraction. This contractile force could be further supported by myosin tethering to cytoskeletal actins, which in turn anchor to the plasma membrane and extracellular matrix through focal adhesion complexes⁴⁷.

The ability of fasudil to inhibit capillary pericyte contraction in our study has two key implications. First, as an inhibitor of Rho-kinase, this drug blocks actomyosin cross-bridge cycling as well as the slower contractile mechanism of actin cytoskeleton polymerization, both of which are known to be important components of SMC contractility. This supports the idea that stimulation of capillary pericytes drives contractile machinery in the cell, rather than nonspecific mechanisms of capillary constriction such as pericyte swelling. With two-photon optogenetic stimulation, the upstream signal leading to Rho-kinase activity may involve ROS, since ROS can cause vasoconstriction via Rho-kinase and NAC was able to block optogenetically induced vasoconstriction. However, the physiological drivers of this contractile pathway in capillary pericytes remain to be clarified. Second, fasudil is clinically used as a treatment to alleviate cerebral vasospasm after subarachnoid hemorrhage in Japan. Studies also show that fasudil treatment improves stroke outcomes in humans⁴⁸ and animals⁴⁹. Our data suggest that one of the many salutary actions of fasudil in these diseases may be prevention of aberrant pericyte contraction and thus improved capillary blood flow.

The observation that not all capillaries respond equally after pericyte ablation is consistent with their role in the creation of basal capillary flow heterogeneity⁵⁰. Capillary pericytes may cooperate with the endothelium to establish varying levels of tone on different capillary segments, which would produce a mixture of low-flux and high-flux vessels within a capillary network. Recent studies have shown that blood flow among brain capillaries homogenizes during functional hyperemia, with capillaries exhibiting low flux at rest experiencing the greatest flow increase during stimulation³⁸. This process is important for distributing the increased blood (and oxygen) that is provided through dilation of upstream arterioles, and changes in capillary pericyte tone may be involved in its coordination⁵⁰. Heterogeneity in capillary pericyte tone may further prioritize blood flow to specific regions under basal conditions. Preferred routes for blood flow, or thoroughfare channels, through the capillary bed have previously been reported in the brain⁵¹, and may be shaped over time by the metabolic needs of the tissue. However, little is known about their functional significance in vivo.

Many recent studies have detected links among pericyte loss, blood flow deficits and brain dysfunction. Yet, the mechanisms driving these relationships remain unclear. Animal studies have shown that genetically induced global pericyte loss/dysfunction leads to hypoperfusion and blood–brain barrier disruption, followed by neurodegeneration^{9,15,19}. However, the numerous deleterious effects of widespread pericyte loss make it difficult to discern exactly how the absence of capillary pericytes alters cerebral blood flow. By ablating individual pericytes in a manner that does not affect the blood–brain barrier³², we isolated the effect of pericyte loss on local blood flow, finding that flow in fact increases in uncovered capillaries (Fig. 6). This finding is in line with our recent study that detected increased blood flow through brain microvessels in a mouse model with mild pericyte deficiency³⁰. How might pericyte loss reported in chronic diseases, such as Alzheimer's disease⁵² and cerebral autosomal dominant arteriopathy with subcortical infarcts and leukoencephalopathy (CADASIL)⁵³, then contribute to cerebral hypoperfusion? Given our finding that capillary flow heterogeneity is stable over days, we suspect that abnormal capillary dilation would disrupt optimized flow patterns and cause imbalanced perfusion and oxygen delivery. This effect would be further compounded by aberrant pericyte constriction caused, for instance, by amyloid- β exposure and oxidative injury, coexisting in the same capillary networks¹⁶. Future studies will be needed to understand how pericyte loss affects capillary network dynamics, and to identify approaches for restoration of pericyte–endothelial contact in the adult brain.

Online content

Any methods, additional references, Nature Research reporting summaries, source data, extended data, supplementary information, acknowledgements, peer review information; details of author contributions and competing interests; and statements of data and code availability are available at <https://doi.org/10.1038/s41593-020-00793-2>.

Received: 19 March 2019; Accepted: 23 December 2020;

Published online: 18 February 2021

References

- Kisler, K., Nelson, A. R., Montagne, A. & Zlokovic, B. V. Cerebral blood flow regulation and neurovascular dysfunction in Alzheimer disease. *Nat. Rev. Neurosci.* **18**, 419–434 (2017).
- Blinder, P. et al. The cortical angiome: an interconnected vascular network with noncolumnar patterns of blood flow. *Nat. Neurosci.* **16**, 889–897 (2013).
- Gould, I. G., Tsai, P. S., Kleinfeld, D. & Linninger, A. The capillary bed offers the largest hemodynamic resistance to the cortical blood supply. *J. Cereb. Blood Flow. Metab.* **37**, 52–68 (2016).
- Grant, R. I. et al. Organizational hierarchy and structural diversity of microvascular pericytes in adult mouse cortex. *J. Cereb. Blood Flow. Metab.* **39**, 411–425 (2017).
- Hill, R. A. et al. Regional blood flow in the normal and ischemic brain is controlled by arteriolar smooth muscle cell contractility and not by capillary pericytes. *Neuron* **87**, 95–110 (2015).
- Armulik, A., Genové, G. & Betsholtz, C. Pericytes: developmental, physiological, and pathological perspectives, problems, and promises. *Dev. Cell* **21**, 193–215 (2011).
- Peppiatt, C. M., Howarth, C., Mobbs, P. & Attwell, D. Bidirectional control of CNS capillary diameter by pericytes. *Nature* **443**, 642–643 (2006).
- Hall, C. N. et al. Capillary pericytes regulate cerebral blood flow in health and disease. *Nature* **508**, 55–60 (2014).
- Kisler, K. et al. Pericyte degeneration leads to neurovascular uncoupling and limits oxygen supply to brain. *Nat. Neurosci.* **20**, 406–416 (2017).
- Cai, C. et al. Stimulation-induced increases in cerebral blood flow and local capillary vasoconstriction depend on conducted vascular responses. *Proc. Natl Acad. Sci. USA* **115**, E5796–E5804 (2018).
- Fernández-Klett, F., Offenhauser, N., Dirnagl, U., Priller, J. & Lindauer, U. Pericytes in capillaries are contractile in vivo, but arterioles mediate functional hyperemia in the mouse brain. *Proc. Natl Acad. Sci. USA* **107**, 22290–22295 (2010).
- Wei, H. S. et al. Erythrocytes are oxygen-sensing regulators of the cerebral microcirculation. *Neuron* **91**, 851–862 (2016).
- Yemisci, M. et al. Pericyte contraction induced by oxidative-nitrative stress impairs capillary reflow despite successful opening of an occluded cerebral artery. *Nat. Med.* **15**, 1031–1037 (2009).
- Montagne, A. et al. Pericyte degeneration causes white matter dysfunction in the mouse central nervous system. *Nat. Med.* **24**, 326–337 (2018).
- Sagare, A. P. et al. Pericyte loss influences Alzheimer-like neurodegeneration in mice. *Nat. Commun.* **4**, 2932 (2013).
- Nortley, R. et al. Amyloid β oligomers constrict human capillaries in Alzheimer's disease via signaling to pericytes. *Science* **365**, eaav9518 (2019).
- Arango-Lievano, M. et al. Topographic reorganization of cerebrovascular mural cells under seizure conditions. *Cell Rep.* **23**, 1045–1059 (2018).
- Li, Y. et al. Pericytes impair capillary blood flow and motor function after chronic spinal cord injury. *Nat. Med.* **23**, 733–741 (2017).
- Nikolakopoulou, A. M. et al. Pericyte loss leads to circulatory failure and pleiotrophin depletion causing neuron loss. *Nat. Neurosci.* **22**, 1089–1098 (2019).
- Vanlandewijck, M. et al. A molecular atlas of cell types and zonation in the brain vasculature. *Nature* **554**, 475–480 (2018).
- Andrasfalvy, B. K., Zemelman, B. V., Tang, J. & Vaziri, A. Two-photon single-cell optogenetic control of neuronal activity by sculpted light. *Proc. Natl Acad. Sci. USA* **107**, 11981–11986 (2010).
- Longden, T. A. et al. Capillary K^+ -sensing initiates retrograde hyperpolarization to increase local cerebral blood flow. *Nat. Neurosci.* **20**, 717–726 (2017).
- Neuhaus, A. A., Couch, Y., Sutherland, B. A. & Buchan, A. M. Novel method to study pericyte contractility and responses to ischaemia in vitro using electrical impedance. *J. Cereb. Blood Flow. Metab.* **37**, 2013–2024 (2016).
- Saponara, S. et al. Effects of commonly used protein kinase inhibitors on vascular contraction and L-type Ca^{2+} current. *Biochem. Pharmacol.* **84**, 1055–1061 (2012).
- Rorsman, N. J. G., Ta, C. M., Garnett, H., Swietach, P. & Tammaro, P. Defining the ionic mechanisms of optogenetic control of vascular tone by channelrhodopsin-2. *Br. J. Pharmacol.* **175**, 2028–2045 (2018).
- Narayanan, D., Xi, Q., Pfeffer, L. M. & Jaggar, J. H. Mitochondria control functional $CaV1.2$ expression in smooth muscle cells of cerebral arteries. *Circ. Res.* **107**, 631–641 (2010).
- Jin, L., Ying, Z. & Webb, R. C. Activation of Rho/Rho kinase signaling pathway by reactive oxygen species in rat aorta. *Am. J. Physiol. Heart Circ. Physiol.* **287**, H1495–H1500 (2004).
- Yoon, J., Choi, M., Ku, T., Choi, W. J. & Choi, C. Optical induction of muscle contraction at the tissue scale through intrinsic cellular amplifiers. *J. Biophotonics* **7**, 597–606 (2014).
- Gutiérrez-Jiménez, E. et al. The effects of hypercapnia on cortical capillary transit time heterogeneity (CTH) in anesthetized mice. *J. Cereb. Blood Flow. Metab.* **38**, 290–303 (2018).
- Watson, A.N. et al. Mild pericyte deficiency is associated with aberrant brain microvascular flow in aged $PDGFR\beta^{+/-}$ mice. *J. Cereb. Blood Flow Metab.* **40**, 2387–2400 (2020).
- Rungta, R. L., Chaigneau, E., Osmanski, B. F. & Charpak, S. Vascular compartmentalization of functional hyperemia from the synapse to the pia. *Neuron* **99**, 362–375 (2018).
- Berthiaume, A. A. et al. Dynamic remodeling of pericytes in vivo maintains capillary coverage in the adult mouse brain. *Cell Rep.* **22**, 8–16 (2018).
- Schmid, F., Reichold, J., Weber, B. & Jenny, P. The impact of capillary dilation on the distribution of red blood cells in artificial networks. *Am. J. Physiol. Heart Circ. Physiol.* **308**, H733–H742 (2015).
- Lyons, D. G., Parpaleix, A., Roche, M. & Charpak, S. Mapping oxygen concentration in the awake mouse brain. *eLife* **5**, e12024 (2016).
- Gutiérrez-Jiménez, E. et al. Effect of electrical forepaw stimulation on capillary transit-time heterogeneity (CTH). *J. Cereb. Blood Flow. Metab.* **36**, 2072–2086 (2016).
- Alarcon-Martinez, L. et al. Interpericyte tunnelling nanotubes regulate neurovascular coupling. *Nature* **585**, 91–95 (2020).
- Li, Y., Wei, W. & Wang, R. K. Capillary flow homogenization during functional activation revealed by optical coherence tomography angiography based capillary velocimetry. *Sci. Rep.* **8**, 4107 (2018).
- Li, B., Lee, J., Boas, D. A. & Lesage, F. Contribution of low- and high-flux capillaries to slow hemodynamic fluctuations in the cerebral cortex of mice. *J. Cereb. Blood Flow. Metab.* **36**, 1351–1356 (2016).
- Stefanovic, B. et al. Functional reactivity of cerebral capillaries. *J. Cereb. Blood Flow. Metab.* **28**, 961–972 (2007).
- Desjardins, M., Berti, R., Lefebvre, J., Dubeau, S. & Lesage, F. Aging-related differences in cerebral capillary blood flow in anesthetized rats. *Neurobiol. Aging* **35**, 1947–1955 (2014).
- Grubb, S. et al. Precapillary sphincters maintain perfusion in the cerebral cortex. *Nat. Commun.* **11**, 395 (2020).

42. Gonzales, A. L. et al. Contractile pericytes determine the direction of blood flow at capillary junctions. *Proc. Natl Acad. Sci. USA* **117**, 27022–27033 (2020).
43. Nelson, A. R. et al. Channelrhodopsin excitation contracts brain pericytes and reduces blood flow in the aging mouse brain in vivo. *Front. Aging Neurosci.* **12**, 108 (2020).
44. Kureli, G. et al. F-actin polymerization contributes to pericyte contractility in retinal capillaries. *Exp. Neurol.* **332**, 113392 (2020).
45. Alarcon-Martinez, L. et al. Retinal ischemia induces α -SMA-mediated capillary pericyte contraction coincident with perivascular glycogen depletion. *Acta Neuropathol. Commun.* **7**, 134 (2019).
46. Alarcon-Martinez, L. et al. Capillary pericytes express α -smooth muscle actin, which requires prevention of filamentous-actin depolymerization for detection. *eLife* **7**, e34861 (2018).
47. Cipolla, M. J., Gokina, N. I. & Osol, G. Pressure-induced actin polymerization in vascular smooth muscle as a mechanism underlying myogenic behavior. *FASEB J.* **16**, 72–76 (2002).
48. Shibuya, M., Hirai, S., Seto, M., Satoh, S. & Ohtomo, E. Effects of fasudil in acute ischemic stroke: results of a prospective placebo-controlled double-blind trial. *J. Neurol. Sci.* **238**, 31–39 (2005).
49. Vesterinen, H. M. et al. Systematic review and stratified meta-analysis of the efficacy of RhoA and Rho kinase inhibitors in animal models of ischaemic stroke. *Syst. Rev.* **2**, 33 (2013).
50. Jespersen, S. N. & Østergaard, L. The roles of cerebral blood flow, capillary transit time heterogeneity, and oxygen tension in brain oxygenation and metabolism. *J. Cereb. Blood Flow. Metab.* **32**, 264–277 (2012).
51. Schmid, F., Tsai, P. S., Kleinfeld, D., Jenny, P. & Weber, B. Depth-dependent flow and pressure characteristics in cortical microvascular networks. *PLoS Comput. Biol.* **13**, e1005392 (2017).
52. Sengillo, J. D. et al. Deficiency in mural vascular cells coincides with blood–brain barrier disruption in Alzheimer’s disease. *Brain Pathol.* **23**, 303–310 (2013).
53. Dziewulska, D. & Lewandowska, E. Pericytes as a new target for pathological processes in CADASIL. *Neuropathology* **32**, 515–521 (2012).

Publisher’s note Springer Nature remains neutral with regard to jurisdictional claims in published maps and institutional affiliations.

© The Author(s), under exclusive licence to Springer Nature America, Inc. 2021

Methods

Animals. The Institutional Animal Care and Use Committee at the Medical University of South Carolina and the Seattle Children's Research Institute approved the procedures used in this study. The institutions have accreditation from the Association for Assessment and Accreditation of Laboratory Animal Care (AAALAC) and all experiments were performed within its guidelines.

To express Chr2-YFP (H134R-eYFP) in mural cells for optogenetic studies, we cross-bred heterozygous PDGFR β -Cre (ref. ⁵⁵) males (FVB/NJ background) with Ai32 females (floxed Chr2-YFP; Jax ID: 024109)⁵⁶. To generate controls for optogenetic studies and for pericyte labeling in ablation studies, we bred heterozygous PDGFR β -Cre males with Ai3 females (floxed YFP; Jax ID: 007903)⁵⁷, or with mT/mG females (floxed membrane-bound eGFP; Jax ID: 007676)⁵⁸. For See Deep Brain (SeeDB) (Fig. 1), auxiliary ablation studies (Fig. 6k–m and Supplementary Figs. 20 and 21) and hypercapnia studies (Fig. 4i–k and Supplementary Fig. 19), we used PDGFR β -tdTomato (ref. ⁵⁹) animals that were generated by crossing heterozygous PDGFR β -Cre males with Ai14 females (Jax ID: 007914). We identified successfully crossed mice by examining for green or red fluorescence in tail tip samples using a fluorescent stereoscope. For all studies we used a roughly equal mixture of both male and female offspring, at ages between 3 and 12 months. The mice were housed on a 12-h light (6:00 to 18:00), 12-h dark cycle, with ad libitum access to chow and water. We did not employ randomized selection strategies for allocation of animals to different experimental groups. However, the use of Chr2-YFP and control mice, or fasudil- or NAC-treated mice with vehicle controls, was interleaved over the entire period of study.

Surgery. We generated acute, skull-removed cranial windows for optogenetic experiments. Under 4% isoflurane anesthesia, we first injected 50 μ l of 0.06 mg ml⁻¹ buprenorphine (0.1 mg kg⁻¹ for a 30-g mouse) intraperitoneally. Once the animal was in the surgical plane of anesthesia (4% MAC induction, 1–2% during surgery), the scalp was excised and the periosteum cleaned from the skull surface. C&B-Metabond quick adhesive cement (Parkell; S380) was then applied to the skull surface to affix a custom-made metal flange to the right half of the skull. This metal flange could later be screwed into a custom holding post for head-fixation during imaging. A 3-mm-diameter circular craniotomy (dura intact) was created over the left hemisphere, and centered over 1.5-mm posterior and 3-mm lateral to bregma, which encompasses the barrel field and other regions of somatosensory cortex. The cortical surface was cleaned of any blood and covered with a drop of warm 1.5% agarose (Sigma; A9793; w/v dissolved in modified artificial cerebral spinal fluid⁶⁰), and immediately overlaid with a 4-mm-diameter glass coverslip (Warner Instruments; 64-0724 (CS-4R)). Care was taken not to compress the cortex during this process, which could affect cortical microvascular flow. Metabond was then used to seal the edges of the coverslip, and to cover any remaining exposed skull surface or skin. We opted to use topical fasudil (Cayman Chemical; 203911-27-7) application, rather than systemic administration. This was done to circumvent fasudil's inability to enter the healthy brain from the bloodstream⁶¹, as well as to avoid confounding reductions in cerebral perfusion pressure that can occur with systemic administration⁶². A fasudil stock solution was diluted directly into the warm 1.5% agarose solution used in the cranial window procedure, providing direct access to the brain through the cortical surface. The final fasudil concentrations in the agarose (1 mM and 10 mM) were chosen based on: (1) previous studies showing that 0.1 mM fasudil prevented constriction of isolated aorta⁶³; and (2) a study showing that ~10% of similarly sized molecules at the meninges enter the brain parenchyma⁶⁴. This was the basis for a 1 mM fasudil concentration. We further included a 10 mM concentration to account for dilution of the fasudil by the brain interstitial fluid⁶⁵. Data collection began roughly 60 min after fasudil/vehicle-loaded agarose application to allow for time to diffuse through the cortex. Similar to fasudil, NAC (Sigma-Aldrich; A9165-25G) was diluted to a concentration of 100 mM into the 1.5% agarose solution for the acute cranial window. This concentration was chosen because 10 mM and 30 mM were effective at preserving contraction and relaxation of isolated coronary arteries after ROS or 800-nm-light exposure, respectively^{28,66}.

For ablation experiments, we generated chronic, skull-removed windows using methods previously described³². Chronic cranial windows were necessary because these experiments required multiple days of follow-up imaging. This is in contrast to the optogenetic studies, which could be performed acutely and required topical drug application in some cases. Chronic window implantation was similar to procedures for acute cranial windows described above, but with the following modifications. A surgical plane of anesthesia was induced with a cocktail consisting of fentanyl citrate (0.05 mg kg⁻¹), midazolam (5 mg kg⁻¹) and dexmedetomidine hydrochloride (0.5 mg kg⁻¹) (all Patterson Veterinary). Dexamethasone (40 μ l; Patterson Veterinary) was also given 4–6 h before surgery, which helped to further reduce brain swelling during the craniotomy. Surgeries were performed under sterile conditions. Craniotomies were sealed with a glass coverslip consisting of a round 3-mm glass coverslip (Warner Instruments; 64-0720 (CS-3R)) glued to a round 4-mm coverslip (Warner Instruments; 64-0724 (CS-4R)) with ultraviolet-cured optical glue (Norland Products; 7110). The coverslip was positioned with the 3-mm side placed directly over the craniotomy, while the 4-mm coverslip laid on the skull surface at the edges of the craniotomy. An instant adhesive (Loctite Instant Adhesive 495) was carefully dispensed along the edge of

the 4-mm coverslip to secure it to the skull, taking care not to allow any spillover onto the brain. Lastly, the area around the cranial window was sealed with dental cement. This two-coverslip 'plug' fits precisely into the craniotomy and helps to inhibit skull regrowth, thereby preserving the optical clarity of the window over months. Imaging was initiated after a 4-week recovery period, when inflammation had subsided.

For hypercapnia experiments, we generated polished and reinforced thinned-skull (PoRTs) windows using previously described methods^{67,68}. This window type does not breach the intracranial space, and therefore avoids potential herniation caused by brain volume change during hypercapnia. Briefly, the skull overlying the sensory cortex was carefully thinned to translucency using a hand-held electrical drill (Osada; EXL-M40) fitted with a 0.5-mm drill burr (Fine Science Tools; 19007-05). The thinned region was cleaned with artificial cerebral spinal fluid and allowed to dry. A drop of Loctite 401 instant adhesive was applied to the dried bone, and immediately overlaid with a 4-mm circular coverslip, taking care to avoid producing bubbles under the glass. The glue was allowed to dry for 15 min, and then the edges of the window were sealed with Metabond. Mice were used for hypercapnia experiments immediately after window implantation.

Distinct cranial window types served different needs in this study. To determine whether window type itself affected cerebral blood flow, we compared basal capillary RBC flux collected from acute and chronic skull-removed cranial windows. RBC flux measured between these two window types was not statistically different, with an average of 69.6 \pm 34.9 cells per second for acute versus 74.9 \pm 47.7 cells per second for chronic (mean \pm s.d.; $P > 0.1$ by Wilcoxon rank-sum test, $n = 87$ capillaries from 9 YFP or mT/mG mice with acute windows; $n = 94$ capillaries from 6 YFP or mT/mG mice with chronic windows).

Two-photon imaging. Optogenetic experiments. Mice were imaged immediately after cranial window construction for optogenetic studies. To label the vasculature, 50 μ l of 2.5% (w/v in saline) 70 kDa Texas red–dextran (Invitrogen; D1830) was injected through the retro-orbital vein under deep isoflurane anesthesia (2% MAC in medical air). Texas red–dextran injections were repeated as needed, roughly every 3 h. Isoflurane was reduced to ~0.8% MAC in medical air, which leaves the mouse anesthetized but reactive to a light toe pinch during imaging. The cortical microvasculature was imaged with a Sutter Moveable Objective Microscope (run by MPscope 2.0) coupled to a Coherent Ultra II Ti:Sapphire laser source. In some studies (relaxation after Chr2 activation, NAC pharmacology and hypercapnia), a different two-photon imaging system was used, consisting of a Bruker Investigator (run by Prairie View 5.5 software) coupled to a Spectra-Physics Insight X3. Green and red fluorescence emission was collected through 515/30-nm and 615/60-nm bandpass filters (525/70-nm and 595/50-nm for Bruker), respectively, and detected by photomultiplier tubes. Low-resolution maps of the cranial window were first collected for navigational purposes using a $\times 4$ (0.16 numerical aperture (NA)) objective (Olympus; UPlanSAPO). We then switched to a $\times 20$ (1.0 NA) water-immersion objective (Olympus; XLUMPLFLN) and imaged with 900-nm excitation to collect volumetric data of individual penetrating arterioles in a way that would not activate Chr2 (lateral resolution 0.63 μ m per pixel, axial resolution 1 μ m). All imaging with the water-immersion lens was done with room-temperature distilled water. The green channel (corresponding to YFP) was used to discern vascular branch order, and to preselect specific pericytes for optogenetic stimulation based on the following criteria: (1) the branch order could be unambiguously discerned; (2) a considerable length of the pericyte was contained within one imaging plane to make line-scanning possible; and (3) the pericyte was not downstream, or within one branch, of a previously stimulated pericyte. We ordered pericyte stimulation from highest (capillaries) to lowest (precapillary arterioles and lastly pial arterioles and venules) branch order. All data in Fig. 4a–h were collected in the same animals. Up to 15 pericytes within the domain of one penetrating arteriole were targeted for optogenetic activation. We only selected penetrating arterioles that extended a primary branch within the upper 300 μ m of cortex. Some higher-order capillaries could be traced to multiple penetrating arterioles as a source. In these cases, the target capillary was categorized based on the lowest branch order from any of the penetrating arterioles. For each mouse, we examined the branching network of one to three penetrating arterioles.

After selecting mural cells for optogenetic stimulation from a large image stack, we used 900-nm excitation (nonstimulating wavelength) to navigate to each of the cells (Supplementary Fig. 3). For each target cell, we first collected a 'pre' image stack (lateral resolution 0.25 μ m per pixel, axial resolution 1 μ m) and a brief video at 900 nm. Images from this video were then used to draw a multi-segmented line-scan path that transected the vessel five times, and bisected the vessel once. This was to acquire multiple measurements of lumen diameter and one measurement of RBC velocity, respectively, as described previously⁶⁹. The pixel dwell time for these line-scan segments was 1.5 μ s. The line-scan was accelerated between these segments to further increase sampling rate. With these parameters we routinely achieved a ~600-Hz sampling rate. We measured the proportion of the line-scan that was fluorescent in the YFP channel, which represents regions where activation of Chr2-YFP could occur. Approximately 8% of the line-scan intersected with Chr2-YFP in capillary scans, that is, 8% duty cycle, and 11% for both precapillary arteriole and pial arteriole scans due to greater vessel coverage

of ensheathing pericytes and SMCs. This slight difference in parameters likely had no effect on outcome, as there was no correlation between duty cycle and the change in vessel diameter when examining each vessel type separately (data not shown), or with all branch orders combined (1st to 9th) ($R = -0.05$, $P = 0.5$ by Pearson's correlation of proportion of scan with YFP versus fold-change diameter, $n = 197$ vessels). For pial arterioles and many precapillary arterioles, a 600-Hz rate could not capture RBC velocity, but could be used to determine vessel diameter. During stimulation, we maintained line-scanning of the target vessel for 60 s at 800-nm excitation, followed by collection of a 'post-stimulation' stack of the same region using 900-nm excitation. Every 2 h of imaging, we injected 200 μ l of lactated Ringer's solution subcutaneously to hydrate the animals (Patterson Veterinary; 07-869-6319). At the conclusion of each experiment, mice were still reactive to a light toe pinch.

The laser powers utilized for the 800-nm- and 900-nm-excitation line-scans were kept consistent across experimental groups by adhering to a power versus cortical depth chart established from preliminary studies on four PDGFR β -Chr2-YFP mice. To further reduce the risk of eliciting vasoconstriction during navigation, or while collecting image stacks, line-scan data were collected at lower laser powers for 900 nm than for 800 nm (Supplementary Figs. 3 and 4). Data collected throughout the study were then added to this dataset, so that comparable levels of laser irradiation at certain depths were applied for all animals (Supplementary Fig. 5). The typical laser powers we used were in the 'high power' groups in Supplementary Figs. 3 and 4. Laser powers were determined at the output of the $\times 20$ objective using a laser power meter (Thor Labs; PM100D), with galvanometric mirrors engaged in a full-field, 512×512 -pixel scan covering $16,600 \mu\text{m}^2$ (0.17 mm^2). Comparable photomultiplier tube gain values were used across all animals. Recent studies by Podgorski and Ranganathan⁷⁰ suggest that irradiation with 800-nm and 920-nm femtosecond laser pulses can increase brain temperature by 1.5 – 3°C after 180 s (ref. ⁷⁰). However, the use of isoflurane, and a room-temperature water objective over a cranial window, decreases brain temperature to about 32 – 33°C (refs. ^{70,71}). This may offset any increase in temperature that may occur during our two-photon irradiation.

For studies using chlorprothixene sedation (Supplementary Fig. 6 and Fig. 4i–k), we injected $30 \mu\text{l}$ of 1 mg ml^{-1} chlorprothixene (Sigma-Aldrich; C1671) solution intramuscularly (thigh muscle), immediately after cranial window surgery with isoflurane. We then injected 70-kDa Texas red-dextran retro-orbitally under 2% isoflurane, turned off the isoflurane and waited 15–30 min for chlorprothixene to take effect. Typically, one injection was sufficient per imaging session. Basal capillary diameter did not differ significantly between isoflurane and chlorprothixene sedation. However, a modest increase in RBC velocity was observed under isoflurane, likely due to upstream arteriole dilation (Supplementary Fig. 6c–f).

The precise mechanism by which two-photon activation of Chr2 causes vasoconstriction remains unclear. Chr2 photocurrent may work in synergy with other effects of high-intensity two-photon light to promote ROS formation and calcium release in mural cells. Enhanced calcium influx and ROS production in Chr2-expressing pericytes may then activate Rho-kinase to promote actomyosin cross-bridging²⁷ and actin polymerization⁷², leading to cell contraction and decrease in capillary flow.

Relaxation after Chr2 activation. Using PDGFR β -Chr2-YFP mice anesthetized with 0.8% MAC isoflurane (separately established and examined at the Seattle Children's Research Institute), we collected full-field videos before, during and after optical stimulation. Videos were collected in regions that: (1) contained a penetrating arteriole with precapillary arteriole offshoot; or (2) contained only capillaries. In the latter, we carefully selected capillary regions with no penetrating or precapillary arterioles within the imaging field to avoid perturbing flow upstream of the imaged capillaries. During continuous video collection, we started with imaging at 900 nm, then switched to 800 nm to stimulate Chr2 for 60 s, and then returned to 900 nm for an additional 450 s to observe vessel relaxation. Videos were collected at ~ 1 frame per second, and imaging resolution was $0.38 \mu\text{m}$ per pixel. Imaging was performed with an Insight X3 laser where power at the output was similar between 800 nm and 900 nm (unlike for line-scans, where we used lower power at 900 nm, as discussed above). Thus, the same laser power (40–50 mW) was applied for both stimulation and observation periods for vessels imaged between 50 and $150 \mu\text{m}$ below the pial surface.

Hypercapnia experiments. PDGFR β -tdTomato mice were sedated with chlorprothixene instead of isoflurane to ensure full capacity for vasodilation, and imaged through a thinned-skull window. Vasculature was labeled with retro-orbital injection of 2-MDa FITC-dextran (Sigma-Aldrich; FD2000S). To ensure the same vessel regions were observed despite shifting due to brain volume change, we collected continuous $25\text{-}\mu\text{m}$ -thick image stacks at a sampling rate of 1 stack every 36 s. Lateral resolution was $0.38 \mu\text{m}$ per pixel and axial resolution was $1 \mu\text{m}$ per pixel. During continuous stack collection, we established a 6-min baseline (10 stacks) during inhalation of air, then 6 min of 5% CO_2 with air balance, delivered through a nose cone placed $\sim 5 \text{ mm}$ from the snout. Finally, we returned to air inhalation for 9 min to observe post-hypercapnic vasoconstriction. Movement artifacts were common during the hypercapnic phase, precluding our

ability to measure rate of vasodilation. However, the mice were calm during the post-hypercapnic phase, allowing quality measurements of vessel diameter. Only vessels without movement artifacts at baseline normocapnia and during the entire recovery phase were considered for analysis. Image registration was used to correct for shifts in the lateral plane (Fiji, StackReg plugin, Rigid body transformation). Diameters were then analyzed as described below.

Ablation experiments. Mice with chronic windows were anesthetized with isoflurane and 70-kDa Texas red-dextran or 2-MDa FITC-dextran was injected to colabel the vasculature, depending on whether PDGFR β -mGFP/YFP or PDGFR β -tdTomato mice were used. Isoflurane was maintained at 0.8% MAC during imaging. On imaging day 1, we collected volumetric data of penetrating arterioles at 900 nm (mGFP/YFP) or 975 nm (tdTomato) excitation with the $\times 20$, 1.0-NA objective. We used these as maps to select pericytes for ablation. Good candidates for ablation: (1) exhibited unambiguous capillary pericyte morphology; and (2) had somata protruding abuminally so as to easily be targeted by the laser without collateral damage to the capillary wall. We then collected high-resolution 'preablation' image stacks of each target capillary (lateral resolution $0.37 \mu\text{m}$ per pixel, axial resolution $1 \mu\text{m}$) and line-scans to gather RBC velocity and flux. After collecting baseline data, we flipped a coin to randomly decide whether the targeted pericytes would be part of the ablation group or sham irradiation control group. We stratified this randomization process so that ablation and control data were collected at comparable depths, and so that the same number of ablation and control cells would be collected from each animal. Further, we ensured that each cell targeted for ablation was more than two capillary branches away from other cells that were targeted for sham or ablation.

To perform pericyte ablation, we used techniques previously described³². Briefly, guided by imaging at the highest digital magnification ($\times 10$; $0.06 \mu\text{m}$ per pixel), we applied a small line-scan restricted to only the soma of the target pericyte (3 – $5 \mu\text{m}$ away from the vessel wall), and scanned this region for 1–3 min using 725-nm excitation at 20–60 mW, depending upon cortical depth. The ablative scan was periodically interrupted to check for successful ablation, which was apparent as loss of fluorescence from the entire cell. Successful ablations resulted in persistent absence of fluorescence from the targeted pericyte, but not in neighboring pericytes, when examined 3 d after ablation. This procedure was similarly applied to ablation of bridging pericytes. For sham irradiation data, we used the same parameters of laser irradiation, but applied the line-scan 3 – $5 \mu\text{m}$ away from the vessel wall at a region lacking pericyte somata. This is the same approximate distance from the vessel wall as when targeting a pericyte soma.

During postablation imaging, we relocated the targeted vessel using vascular architecture for guidance. Image stacks and line-scans of the same capillary were collected with identical parameters as at baseline. In four mice, we also ablated (or sham-irradiated) two adjacent pericytes to examine whether the amount of uncovered capillary length influenced the extent of hemodynamic change postablation (Fig. 6a,b). However, we found no difference in capillary hemodynamics whether one or two pericytes were ablated (data not shown), and the ablation data were therefore combined.

Analysis of in vivo imaging data. Pericyte coverage. Capillary regions of interest were first defined in the i.v. dye channel from image stacks collected at $0.25\text{-}\mu\text{m}$ per pixel lateral resolution. Then, in the second channel (Chr2-YFP, YFP or mGFP), the area of pericyte coverage in the region of interest was identified by thresholding in ImageJ/Fiji. The area fraction of pixels above this threshold was obtained and reported as percentage coverage of the capillary. The same threshold level was applied to all capillaries examined, and analyses were performed with the rater blinded to genotype (Supplementary Fig. 1).

Determining vessel depth. We calculated the cortical depth of all stimulated vessels by browsing the initial $300 \mu\text{m}$ of cortical depth in image stacks of the penetrating arteriole network using ImageJ/Fiji. We measured the distance between the bottom of the dura mater and the plane in which the line-scan for a single vessel was performed. This was facilitated by YFP or GFP labeling of meningeal fibroblasts in the dura with use of PDGFR β -Cre mice.

Automated analysis of vessel diameter and RBC velocity from line-scan data. For each line-scan in our optogenetic studies, we calculated the diameter from all five diameter lines by measuring the full-width at half-maximum of the vessel's intensity profile, as previously described^{60,69}. The spatial resolution of the diameter scans was $\sim 0.5 \mu\text{m}$ per pixel. Linear interpolation was used to add subpixel accuracy to the diameter measurement. We calculated RBC velocity from the single bisecting line-scan using the radon transform method, as previously described⁷³. The window of data used for analysis of both diameter and RBC velocity was 40 ms (average of ~ 24 lines). Time-course data were acquired by running this window along the length of the line-scan, with 20-ms overlap between windows, providing 50 measurements per second. We then processed these raw diameter and RBC velocity values in batches using custom MATLAB scripts. During this process, we filtered out extreme RBC velocity values by converting values greater than three times the standard deviation into the mean of the entire trace. Then, for unbiased quality control, the mean of the diameter trace had to be greater than the

standard deviation for the data to be analyzed using automation. Typically, four of the five collected diameter traces passed this criterion, and these traces were averaged together. The occasional presence of a stalled RBC prevented the ability to obtain a diameter calculation, and these traces were excluded. In instances where a 'fold-change' in diameter or RBC velocity was provided, this was calculated by dividing the averaged value from 58–60 s in the line-scan by the average of 0–3 s, the latter being considered our baseline. The time-course traces shown in the figures using line-scan are median-filtered over 1 s, but median-filtered data were not used to calculate fold-changes used in statistical comparisons. For the ablation experiments, we analyzed the RBC velocity in the same manner as for optogenetic studies, explained above. RBC velocities for ablation experiments were reported as the average of a 60-s line-scan collected at 900-nm excitation.

Automated analysis of vessel diameter in full-field or maximally projected images. Lumen diameter was measured in full-field images for ablation, postoptogenetic relaxation and hypercapnic studies. The two-dimensional images or videos were anonymized to blind the rater (D.A.H., T.T. or A.Y.S.) to the experimental group. To reduce bias of measurement location, we used a custom ImageJ/Fiji macro called VasoMetrics⁵⁴ to analyze lumen diameter at multiple, equidistant locations along each vessel segment of interest. The user first draws a line that bisects the vessel segment to be measured. The macro then creates perpendicular cross-lines (spaced ~3 μm) to obtain fluorescence intensity across the lumen width. It then calculates the full-width at half-maximum of the intensity profile for each equidistant location. These values were then averaged together and converted to micrometer units to obtain a single diameter value per vessel segment. In cases where RBC flow measurements had also been collected for the same vessel, the initial bisecting line was drawn to match where RBC flow line-scan measurements were collected.

Rate of diameter change. Continuous diameter data from individual vessels were linearly regressed in MATLAB software to calculate the rate of absolute diameter change. We focused on periods where the kinetics between ensheathing versus capillary pericytes were clearly distinct and in a roughly linear phase of change. In optogenetic constriction data, this was the first 10 s after initiation of optogenetic stimulation for both cell types. In hypercapnia data, this was the first ~144 s of data after transition to normocapnia for both cell types. In data collected for relaxation after Chr2 activation, the time range examined was different for ensheathing and capillary pericytes due to their distinct kinetics. Rate was calculated in the first 50 s following the optogenetic stimulation phase for ensheathing pericytes, and from 50 to 400 s for capillary pericytes.

Analysis of flow–no flow and membrane blebbing in post-stacks. We visually examined all postablation image stacks in a blinded and randomized manner. Image stacks from all experimental groups were gathered and randomized for analysis using a random number generator in custom MATLAB code. We scrolled through each image stack and categorized them for blood flow through the stimulated capillary segment. We denoted capillaries as 'flowing' if there was any movement of RBC shadows between frames of the image stack. In a blinded manner, we also tallied the presence of pericyte membrane 'blebbing', defined as focal, bubble-like protrusions from the stimulated pericyte that were not present before the stimulation period.

Manual analysis of RBC velocity. Automated analysis of RBC velocity was inaccurate for cases that slowed greatly or stopped flowing altogether⁷³. Therefore, whenever the standard deviation exceeded the mean RBC velocity, we manually analyzed the RBC velocity (44 of 175 Chr2-YFP versus 2 of 161 control, for branch orders 5–9). To do this, we compared the slope of RBC streaks in one frame at the beginning of the line-scan, and in one frame at the end. We reduced bias by blinding the rater (D.A.H.) to the timing of the presented frames (beginning or end of scan). We calculated: (1) the distance traveled by RBCs (*x* dimension) using a pixel per micrometer conversion for the line-scan; and (2) time of travel (*y* dimension) using the line-sampling rate; and divided these values to derive RBC velocity. Of note, manual RBC velocity analyses were only used in calculating fold-change to increase accuracy for statistics. Continuous RBC velocity traces presented in the figures did not exclude any data based on high standard deviation.

Quantification of RBC flux. The line-scan data from optogenetic or ablation studies were cropped to show only the part of the scan where velocity was measured. We then manually counted the number of blood cell streaks occurring in frames at 1, 30 and 60 s of the line-scan using a custom-made MATLAB script. These frames were presented to the rater (D.A.H.) in random order, and blind to the group, to reduce bias. Some streaks appeared thicker and likely corresponded to a rouleau of RBCs. These streaks were counted as single RBCs since it was not possible to distinguish the number of cells, which may lead to a slight underestimation of the RBC count. Line-scans were excluded from analysis if the RBC flux was too high for reliable cell counting (Supplementary Fig. 12) or if the RBCs were stuck together for more than ~20% of the presented frame (50 of 168 Chr2-YFP scans and 61 of 148 YFP scans were excluded under these criteria). For optogenetic data, RBC flux counts at 30 and 60 s were then normalized to counts at 1 s to provide a

fold-change from baseline. For pericyte ablation data, RBC flux values at 1, 30 and 60 s were averaged together to provide a single value for each capillary in a given day.

Image processing. Only raw images were utilized in data analysis, viewed with ImageJ/Fiji v.1.0 or MATLAB software. For presentation purposes, images were contrasted and cropped in Adobe Photoshop, one color channel at a time, in a similar manner across all conditions.

Exclusion criteria. For optogenetic experiments, we omitted data from any capillaries with visible Texas red–dextran extravasation in the post-stimulation image stack. Diameter data were excluded if the baseline diameter was less than 1 μm. If precise depth could not be calculated for a capillary, we did not include that capillary in plotting laser power versus cortical depth. In ablation datasets, we excluded cells that were not successfully ablated, or if neighboring processes had already grown into the previously uncovered region, at 3 d postablation. For hypercapnia experiments, we excluded vessels that dilated less than 5% above baseline levels, as the magnitude of constriction was too small for reliable rate calculation.

Histology. Thin sections. Isolated pericytes were examined as shown in Fig. 1g,h. As previously described⁴, NG2-Ai14 mice were deeply anesthetized with euthasol (Patterson Veterinary; 07-805-9296), and then transcardially perfused with PBS, followed by 4% paraformaldehyde (PFA) in PBS. After perfusion, the brain was extracted and incubated in 4% PFA in PBS overnight. Brains were then transferred to PBS with 0.01% sodium azide (w/v, Sigma-Aldrich; S2002), where they were stored until being sliced on a Vibratome Series 1000. We performed antigen retrieval by placing sections into a vial of 0.125% trypsin (Sigma; T4049) in PBS, and incubating the vial at 37 °C for 1 h. Afterwards, FITC-conjugated tomato lectin (1:250 dilution; Vector Laboratories; FL-1171) and anti- α -SMA antibody (1:200 dilution; mouse host, Sigma-Aldrich; A5228) were added to an incubation solution composed of 2% TritonX-100 (v/v, Sigma-Aldrich; X100), 10% goat serum (v/v, Vector Laboratories; S1000) and 0.1% sodium azide (w/v) in PBS. After overnight incubation, the slices were washed in PBS, and then the slices were added to incubation solution containing anti-mouse Alexa 647 secondary antibody (1:500 dilution; ThermoFisher; A31626) for 2 h. Slices were washed in PBS, then mounted onto a slide, dried and sealed with a coverslip using Fluoromount G (Southern Biotech; 0100-01). We collected images for green, red and far-red emission using an Olympus BX61 confocal microscope with a UPLSAPO10x2 objective lens (0.345 pixels-per-micrometer lateral resolution, 1-μm z-step size) and a UPLSAPO 60xO objective lens (8.8 pixels-per-micrometer lateral resolution, 1-μm z-step size).

Optical clearing and two-photon imaging of thick brain sections. To measure capillary pericyte territory in the cortical vasculature, we used the same optical clearing and imaging methods described previously⁴. Briefly, a vibratome was used to cut 500-μm-thick coronal sections of PDGFR β -tdTomato brains. These sections included the somatosensory cortex based on visible landmarks and a mouse brain atlas. Trypsin antigen retrieval was performed for 1 h, as described for thin sections. The tissues were then incubated in anti- α -SMA-FITC antibody (1:200; Sigma; F3777) in the same incubation solution described above for 1 week, and then rinsed in PBS for 1 h. The SeeDB optical tissue clearing method was then performed⁴. After the 5-d SeeDB protocol, the sections were submerged in SeeDB solution and imaged with two-photon microscopy. Four large image stacks were collected from sensory cortex, each encompassing a volume of 0.055 mm³, with dimensions of 500 μm in anterior-posterior direction (corresponding to coronal slice thickness), 312 μm in medial-lateral direction and 350 μm of depth from the pial surface. Only the upper 350 μm of cortex was analyzed, as it corresponded with our *in vivo* imaging capabilities. The image stacks were stitched together with the XuvTools⁷⁵ (www.xuvtools.org) and further examined in Imaris software (Bitplane). The total length of microvasculature was then manually traced in three dimensions using Imaris, and the proportion exhibiting tdTomato or anti- α -SMA-FITC fluorescence was determined. For calculations of branch order of α -SMA termination, we analyzed the datasets as described previously, but reported α -SMA termination of each vessel branch, rather than averaging branch orders per penetrating arteriole offshoot⁴.

Statistics and reproducibility. Calculations and statistical tests were performed in MATLAB (R2018a), SAS v.9.4 or R v.3.5.1. No statistical methods were used to predetermine sample sizes but our sample sizes are similar to those reported in previous publications^{20,32}. Main figures: fold-change values of vessel diameter, RBC velocity and RBC flux were compared across groups using either a repeated-measures analysis of variance (ANOVA) model or a linear mixed-effects model, with genotype, drug/vehicle or ablation/sham group as covariables in the model. A random intercept was included in all models to account for differences across animals. This strategy considers the nested nature of the data; that is, that multiple vessels come from one animal and are thus not independent of one another. A two-way repeated-measures ANOVA was used when comparing relative diameter change on both vessel type and genotype. A linear mixed-effects model

was used in comparing rate of constriction after hypercapnia and rate of vessel dilation after optogenetic stimulation for precapillary arterioles and capillaries. A repeated-measures ANOVA was used in comparing the effect of pericyte ablation on small and large vessels. Post hoc comparisons were made using a Tukey post hoc adjustment, where applicable. Data for the fold-change in RBC velocity and flux after ablation, as well as rate of diameter change after optogenetic stimulation and hypercapnia, were right-skewed and log-transformed before running analyses. All statistical tests were two-tailed. *N* values in the figure legends represent repetitions of the same experimental conditions. Example images were chosen to best represent the group average. For the supplementary figures, details of statistical tests used are described within the figure legends.

Reporting Summary. Further information on research design is available in the Nature Research Reporting Summary linked to this article.

Data availability

Source data are provided with this paper. Any additional data are available from the corresponding author upon request.

Code availability

Vasometrics⁵⁴, an ImageJ/Fiji-based macro for unbiased vessel diameter measurement, can be downloaded at: <https://github.com/mcdowellkonnor/ResearchMacros>. All other code is available from the corresponding author upon request.

References

54. McDowell, K. P., Berthiaume, A. A., Tieu, T., Hartmann, D. A. & Shih, A. Y. VasoMetrics: unbiased spatiotemporal analysis of microvascular diameter in multi-photon imaging applications. *Quant. Imaging Med. Surg.* **11**, 969–982 (2021).
55. Cuttler, A. S. et al. Characterization of Pdgfrb-Cre transgenic mice reveals reduction of ROSA26 reporter activity in remodeling arteries. *Genesis* **49**, 673–680 (2011).
56. Madisen, L. et al. A toolbox of Cre-dependent optogenetic transgenic mice for light-induced activation and silencing. *Nat. Neurosci.* **15**, 793–802 (2012).
57. Madisen, L. et al. A robust and high-throughput Cre reporting and characterization system for the whole mouse brain. *Nat. Neurosci.* **13**, 133–140 (2010).
58. Muzumdar, M. D., Tasic, B., Miyamichi, K., Li, L. & Luo, L. A global double-fluorescent Cre reporter mouse. *Genesis* **45**, 593–605 (2007).
59. Hartmann, D.A. et al. Pericyte structure and distribution in the cerebral cortex revealed by high-resolution imaging of transgenic mice. *Neurophotonics* **2**, 041402 (2015).
60. Shih, A. Y. et al. Two-photon microscopy as a tool to study blood flow and neurovascular coupling in the rodent brain. *J. Cereb. Blood Flow. Metab.* **32**, 1277–1309 (2012).
61. Chen, M. et al. Simply combining fasudil and lipoic acid in a novel multitargeted chemical entity potentially useful in central nervous system disorders. *RSC Adv.* **5**, 37266–37269 (2014).
62. Shin, H. K. et al. Rho-kinase inhibition acutely augments blood flow in focal cerebral ischemia via endothelial mechanisms. *J. Cereb. Blood Flow. Metab.* **27**, 998–1009 (2007).
63. Asano, T. et al. Mechanism of action of a novel antivasospasm drug, HA1077. *J. Pharmacol. Exp. Ther.* **241**, 1033–1040 (1987).
64. Roth, T. L. et al. Transcranial amelioration of inflammation and cell death after brain injury. *Nature* **505**, 223–222 (2014).
65. Bedussi, B. et al. Clearance from the mouse brain by convection of interstitial fluid towards the ventricular system. *Fluids Barriers CNS* **12**, 23 (2015).
66. Rodrigues, A. J., Evora, P. R. & Schaff, H. V. Protective effect of N-acetylcysteine against oxygen radical-mediated coronary artery injury. *Braz. J. Med. Biol. Res.* **37**, 1215–1224 (2004).
67. Drew, P. J. et al. Chronic optical access through a polished and reinforced thinned skull. *Nat. Methods* **7**, 981–984 (2010).
68. Shih, A. Y., Mateo, C., Drew, P. J., Tsai, P. S. & Kleinfeld, D. A polished and reinforced thinned skull window for long-term imaging and optical manipulation of the mouse cortex. *J. Vis. Exp.* **7**, 3742 (2012).
69. Driscoll, J. D., Shih, A. Y., Drew, P. J., Cauwenberghs, G. & Kleinfeld, D. Two-photon imaging of blood flow in cortex. *Cold Spring Harb. Protoc.* **8**, 759–767 (2013).
70. Podgorski, K. & Ranganathan, G. Brain heating induced by near-infrared lasers during multiphoton microscopy. *J. Neurophysiol.* **116**, 1012–1023 (2016).
71. Roche, M. et al. In vivo imaging with a water immersion objective affects brain temperature, blood flow and oxygenation. *eLife* **8**, e47324 (2019).
72. Xu, Q., Huff, L. P., Fujii, M. & Griendling, K. K. Redox regulation of the actin cytoskeleton and its role in the vascular system. *Free Radic. Biol. Med.* **109**, 84–107 (2017).
73. Drew, P. J., Blinder, P., Cauwenberghs, G., Shih, A. Y. & Kleinfeld, D. Rapid determination of particle velocity from space-time images using the Radon transform. *J. Comput. Neurosci.* **29**, 5–11 (2010).
74. Ke, M. T., Fujimoto, S. & Imai, T. SeeDB: a simple and morphology-preserving optical clearing agent for neuronal circuit reconstruction. *Nat. Neurosci.* **16**, 1154–1161 (2013).
75. Emmenlauer, M. et al. XuvTools: free, fast and reliable stitching of large 3D datasets. *J. Microsc.* **233**, 42–60 (2009).

Acknowledgements

Our work is supported by grants to A.Y.S. from the NIH/NINDS (grant nos. NS106138, NS097775) and the NIH/NIA (AG063031, AG062738), by the American Heart Association (grant no. 14GRNT20480366), by the Alzheimer's Association NIRG award (grant no. 2016-NIRG-397149) and by an Institutional Development Award (IDeA) from the NIGMS under grant no. P20GM109040. D.A.H. is supported by awards from the NIH/NCATS (grant nos. UL1 TR001450 and TL1 TR001451) and by NIH/NINDS grant no. F30NS096868. We thank J. Costello for contributions to image analysis. We appreciate the helpful comments and discussion of M. Levy, D. Kleinfeld, A. Riegel, P. Kara and N. Bhat.

Author contributions

Experiments were designed by A.Y.S., D.A.H. and A.-A.B. Experiments were conducted by D.A.H., A.-A.B., R.I.G., S.A.H., T.K. and A.Y.S. Data analysis was performed by D.A.H., A.-A.B., S.A.H., T.K., T.T., K.P.M. and A.Y.S. Statistics were performed by A.L.K., A.V.F. and D.A.H. The manuscript was written by A.Y.S. and D.A.H. with contributions from all authors.

Competing interests

The authors declare no competing interests.

Additional information

Supplementary information The online version contains supplementary material available at <https://doi.org/10.1038/s41593-020-00793-2>.

Correspondence and requests for materials should be addressed to A.Y.S.

Peer review information *Nature Neuroscience* thanks David Bennett, Turgay Dalkara and the other, anonymous, reviewer(s) for their contribution to the peer review of this work.

Reprints and permissions information is available at www.nature.com/reprints.

Reporting Summary

Nature Research wishes to improve the reproducibility of the work that we publish. This form provides structure for consistency and transparency in reporting. For further information on Nature Research policies, see [Authors & Referees](#) and the [Editorial Policy Checklist](#).

Statistics

For all statistical analyses, confirm that the following items are present in the figure legend, table legend, main text, or Methods section.

n/a Confirmed

- The exact sample size (n) for each experimental group/condition, given as a discrete number and unit of measurement
- A statement on whether measurements were taken from distinct samples or whether the same sample was measured repeatedly
- The statistical test(s) used AND whether they are one- or two-sided
Only common tests should be described solely by name; describe more complex techniques in the Methods section.
- A description of all covariates tested
- A description of any assumptions or corrections, such as tests of normality and adjustment for multiple comparisons
- A full description of the statistical parameters including central tendency (e.g. means) or other basic estimates (e.g. regression coefficient) AND variation (e.g. standard deviation) or associated estimates of uncertainty (e.g. confidence intervals)
- For null hypothesis testing, the test statistic (e.g. F , t , r) with confidence intervals, effect sizes, degrees of freedom and P value noted
Give P values as exact values whenever suitable.
- For Bayesian analysis, information on the choice of priors and Markov chain Monte Carlo settings
- For hierarchical and complex designs, identification of the appropriate level for tests and full reporting of outcomes
- Estimates of effect sizes (e.g. Cohen's d , Pearson's r), indicating how they were calculated

Our web collection on [statistics for biologists](#) contains articles on many of the points above.

Software and code

Policy information about [availability of computer code](#)

Data collection

All data collected with MPScope 2.0 (Nguyen, et al. <https://www.ncbi.nlm.nih.gov/books/NBK20235/>), downloaded from <https://neurophysics.ucsd.edu/software.php> to run the Sutter Moveable Objective two-photon microscope. In separate experiments, we used Prairie View 5.5 software to run a Bruker Investigator two-photon microscope.

Data analysis

MATLAB version 2014 or 2017 with image processing toolboxes were used. Data were visualized with Adobe Photoshop CS6, Imaris Bitplane 7.6.5, ImageJ/Fiji ver. 1.0.

For manuscripts utilizing custom algorithms or software that are central to the research but not yet described in published literature, software must be made available to editors/reviewers. We strongly encourage code deposition in a community repository (e.g. GitHub). See the Nature Research [guidelines for submitting code & software](#) for further information.

Data

Policy information about [availability of data](#)

All manuscripts must include a [data availability statement](#). This statement should provide the following information, where applicable:

- Accession codes, unique identifiers, or web links for publicly available datasets
- A list of figures that have associated raw data
- A description of any restrictions on data availability

There are no restrictions on data from this study. Source data used to generate graphs for Main and Supplementary Figures are available in the Supplementary Materials. Any additional data are available from the corresponding author upon request.

Field-specific reporting

Please select the one below that is the best fit for your research. If you are not sure, read the appropriate sections before making your selection.

Life sciences Behavioural & social sciences Ecological, evolutionary & environmental sciences

For a reference copy of the document with all sections, see [nature.com/documents/nr-reporting-summary-flat.pdf](https://www.nature.com/documents/nr-reporting-summary-flat.pdf)

Life sciences study design

All studies must disclose on these points even when the disclosure is negative.

Sample size	No statistical methods were used to pre-determine sample sizes but our sample sizes are similar to those reported in previous publications (PMID: 29298435, 31987006).
Data exclusions	For optogenetic experiments, we omitted data from any capillaries with visible Texas red-dextran extravasation in the post-stimulation image stack (10/213 capillaries in Chr2-YFP group). This indicated laser damage to the capillary. Diameter data were excluded if the baseline diameter was less than 1 μm (5/213 capillaries in Chr2-YFP). This is because the vessel would be too small for reliable calculation of diameter change. If precise imaging depth could not be calculated, then we did not include that capillary in plotting laser power versus cortical depth. In pericyte ablation data sets, we excluded cells that were not successfully ablated 3-days post-ablation (3/41 pericytes). In several cases (7/41 ablations, 18 capillary segments), it was clear that the original pericyte was successfully ablated and new processes had grown into the region where we collected diameter and blood flow—these segments were not included in ablation data sets, because tone was re-established by neighboring pericytes. Six surgerized animals were excluded for either excessive bleeding in the window (2 Chr2, 2 YFP), or for cloudy imaging field (2 mTmG for ablation experiments). Collectively, these are common practices for data exclusion in two-photon imaging studies.
Replication	For optogenetic data (e.g. Figs. 2, 4), we replicated the core results 2 years apart at the Medical University of South Carolina. The initial dataset was Chr2 vs YFP animals n=5 per group. The replication dataset, collected 2 years later, was with a separate cohort of 5 Chr2 animals, and compared them to 4 mT/mG animals. The replication cohorts were started with new breeders from Jackson Labs. Experiments on each animal were performed as similarly as possible. We again replicated the finding of optogenetic capillary pericyte contraction (Fig. 5) 4 years after the initial data set at a different Institute (Seattle Children's) using new breeders and a different two-photon imaging system. The ablation experiments are primarily a replication of other experiments our lab has published, performed by a different lab member, with the advancement that here we measure blood flow changes in detail (PMID 29298435). All attempts at replication were successful.
Randomization	No formal randomization was used for selecting animals for surgery and imaging. We used mice with the appropriate transgenic cross as they became available from cross-breedings. This made randomization difficult, for instance, if it so happened that only males in one litter expressed Chr2-YFP. Covariates were controlled by ensuring proportions of males and females were not significantly different between groups (8/10 chr2 were male, 5/9 ctrl animals were male, $p=0.5155$ on Chi-square test). Additionally, age of mice was not significantly different between groups (121 days old on average in Chr2, 108 days old on average in control). Comparing the changes in capillary diameter from males only between Chr2 and controls shows average fold change diameter 0.95 (ctrl) vs 0.79 (chr2), $p=7.0713e-13$ by Wilcoxon rank-sum test, very similar to overall results that included females. Covariates were controlled for in ablation studies because ablation and sham data were collected from the exact same mice. Data were randomized for analysis by first compiling data from all different comparison groups together, then having MATLAB blindly assign each image file a random number. Analysis then proceeded in numerical order.
Blinding	Surgeries were performed and data were collected in an unblinded manner. This is because the morphology of cells is different between genotypes and it is impossible to blind oneself to the genotype while imaging (Supp Fig 1). However, all analyses were performed with the rater blinded to the conditions (e.g. the genotype, ablation/sham, and if the data represented the baseline or follow up). In addition, statisticians performing the primary analyses were blinded to the hypothesis and group identification.

Reporting for specific materials, systems and methods

We require information from authors about some types of materials, experimental systems and methods used in many studies. Here, indicate whether each material, system or method listed is relevant to your study. If you are not sure if a list item applies to your research, read the appropriate section before selecting a response.

Materials & experimental systems

n/a	Involved in the study
<input type="checkbox"/>	<input checked="" type="checkbox"/> Antibodies
<input checked="" type="checkbox"/>	<input type="checkbox"/> Eukaryotic cell lines
<input checked="" type="checkbox"/>	<input type="checkbox"/> Palaeontology
<input type="checkbox"/>	<input checked="" type="checkbox"/> Animals and other organisms
<input checked="" type="checkbox"/>	<input type="checkbox"/> Human research participants
<input checked="" type="checkbox"/>	<input type="checkbox"/> Clinical data

Methods

n/a	Involved in the study
<input checked="" type="checkbox"/>	<input type="checkbox"/> ChIP-seq
<input checked="" type="checkbox"/>	<input type="checkbox"/> Flow cytometry
<input checked="" type="checkbox"/>	<input type="checkbox"/> MRI-based neuroimaging

Antibodies

Antibodies used	Monoclonal alpha-smooth muscle actin-FITC conjugated (Sigma F3777); Monoclonal alpha-smooth muscle actin primary (Sigma A5228); Secondary antibody rabbit anti-mouse Alexa 594 (Invitrogen A27027).
Validation	The same clones were validated in a study by Tomasek, et al. which found no antibody staining in aSMA knockout tissue (https://www.ncbi.nlm.nih.gov/pmc/articles/PMC3540133/).

Animals and other organisms

Policy information about [studies involving animals](#); [ARRIVE guidelines](#) recommended for reporting animal research

Laboratory animals	All animals were offspring of male PDGFRBeta-Cre mice, a generous gift from Volkhard Lindner, on the FVB/NJ background (https://www.ncbi.nlm.nih.gov/pubmed/21557454). These males were crossed with females from Jackson labs that were Ai32 (ChR2-YFP; Jax ID 024109), Ai3 (eYFP; Jax ID 007903), or mT/mG (membrane-bound eGFP; Jax ID 007676) on a C57/BL6 background. Male and female F1 offspring were used for experiments, between ages 3-12 months. Groups were not different according to the distribution of mouse age or gender, and there were no trends in the data pointing towards an animal sex or age effect (data not shown). Animal room conditions: Temp = 71.8 -72 (DEGF), Humidity = 38.6 (% RH) Pressure = 0.006 (in WG).
Wild animals	This study did not involve wild animals.
Field-collected samples	This study did not involve wild animals or field samples.
Ethics oversight	The Institutional Animal Care and Use Committee at the Medical University of South Carolina and the Seattle Children's Research Institute approved the procedures used in this study. The institutions have accreditation from AAALAC and all experiments were performed within its guidelines.

Note that full information on the approval of the study protocol must also be provided in the manuscript.